JOURNAL OF GEOPHYSICAL RESEARCH, VOL. 108, NO. D17, 4534, doi:10.1029/2003JD003470, 2003

Empirical TOMS index for dust aerosol: Applications to model validation and source characterization

Paul Ginoux[1]

Goddard Earth Sciences and Technology, University of Maryland Baltimore County, and NASA Goddard Space Flight Center, Greenbelt, Maryland, USA

Omar Torres

Joint Center for Earth Systems Technology, University of Maryland Baltimore County, and NASA Goddard Space Flight Center, Greenbelt, Maryland, USA

Received 30 January 2003; revised 21 May 2003; accepted 10 June 2003; published 4 September 2003.

[1] An empirical relation is developed to express the Total Ozone Mapping Spectrometer (TOMS) aerosol index (AI) for the case of dust plumes, as an explicit function of four physical quantities: the single scattering albedo, optical thickness, altitude of the plume and surface pressure. This relation allows sensitivity analysis of the TOMS AI with physical properties, quantitative comparison with dust model results and physical analysis of dust sources, without the necessity of cumbersome radiative calculation. Two applications are presented: (1) the case study of a dust storm over the North Atlantic in March 1988, and (2) the characterization of 13 major dust sources. The first application shows that simulated dust distribution can be quantitatively compared to TOMS AI on a daily basis and over regions where dust is the dominant aerosol. The second application necessitates to further parameterize the relation by replacing the optical thickness and the altitude of the plume by meteorological variables. The advantage is that surface meteorological fields are easily available globally and for decades but the formulation only applies to dust sources. The daily, seasonal and interannual variability of the parameterized index over major dust sources reproduces correctly the variability of the observed TOMS AI. The correlation between these two indices is used to determine the surface characteristics and physical properties of dust aerosol over the sources. *INDEX TERMS:* 0305 Atmospheric Composition and Structure: Aerosols and particles (0345, 4801); 0322 Atmospheric Composition and Structure: Constituent sources and sinks; 0360 Atmospheric Composition and Structure: Transmission and scattering of radiation; 0368 Atmospheric Composition and Structure: Troposphere—constituent transport and chemistry; *KEYWORDS:* dust sources, dust modeling, TOMS satellite

Citation: Ginoux, P., and O. Torres, Empirical TOMS index for dust aerosol: Applications to model validation and source characterization, *J. Geophys. Res.*, *108*(D17), 4534, doi:10.1029/2003JD003470, 2003.

1. Introduction

[2] Wind erosion in arid and semi-arid regions produces massive airborne plumes of dust particles which affect the Earth's climate system. Due to their optical properties, dust particles could play an important role in the radiation energy balance and climate forcing [*Tegen and Lacis*, 1996; *Sokolik and Toon*, 1996], and tropospheric chemistry by reducing the photolysis rates [*Dickerson et al.*, 1997; *Liao et al.*, 1999]. Dust particles provide reaction sites for ozone and nitrogen molecules [*Prospero et al.*, 1995; *Dentener et al.*, 1996; *Martin et al.*, 2002]. Dust deposition at the ocean surface is a source of nutrients, and could be the main source of iron for phytoplankton blooming in the open oceans [*Martin and Gordon*, 1988]. Finally, dust particles affect air quality [*Prospero*, 1999] and are potential vectors for long range transport of bacteria [*Prospero et al.*, 2003]. However, the accurate evaluation of these effects remain uncertain due to the lack of detailed information on the size distribution, mineralogical composition, atmospheric transport and removal processes, and more fundamentally the sources location and strength of dust emissions. To study dust sources, satellite instruments provide the most useful data sets with their global coverage and long term daily observations. Among these instruments, the Total Ozone Mapping Spectrometer (TOMS) has the particularity to measure backscattering radiances in the near ultra-violet (nUV). The advantage of the nUV technique is that aerosol properties can be derived on both land and ocean due to low surface reflectance in the nUV [*Herman and Celarier*, 1997]. The TOMS nUV radiances have been used to derive an aerosol index (AI) which provides daily and global information on the distribution of absorbing aerosols. Since, the TOMS AI has been used for multiple applications: to analyze the global

[1]Now at Geophysical Fluid Dynamics Laboratory, NOAA, Princeton, New Jersey, USA.

0148-0227/03/2003JD003470$09.00

distribution of absorbing aerosol [*Herman et al.*, 1997], to study the aerosol properties [*Torres et al.*, 1998, 2002], to calculate the radiative forcing of Saharan dust [*Hsu et al.*, 2000], to study the variability of Saharan dust transport over the Atlantic [*Chiapello and Moulin*, 2002], to initialize forecasting model of dust aerosol [*Alpert et al.*, 2002], to identify the location and geo-morphological characteristics of dust sources [*Prospero et al.*, 2002], to establish a global dust source function for transport model [*Ginoux et al.*, 2001], and validate dust distribution at the regional and global scale [*Ginoux et al.*, 2003].

[3] The quantitative use of the TOMS aerosol index to characterize source strength is limited by its lack of direct representation of aerosol macrophysical properties: optical thickness and single scattering albedo. These properties can been derived by using complex radiative calculations if the vertical distribution and size distribution can be obtained from an independent data set [*Torres et al.*, 2002]. This paper examines the possibility to use an empirical function based on these radiative calculations which express explicitly the TOMS AI as a function of optical thickness, single scattering albedo and altitude of the plume for the case of dust aerosols. The advantages are that such relation provides direct comparison between simulation of dust plumes and satellite data, and may further improve our understanding of dust emission. After analyzing the error associated with each variables of this first empirical function of TOMS AI, $\overline{AI}$, we show how it can be applied (1) to validate simulated dust distributions and (2) to characterize dust sources. For this second application, a new relationship, $\overline{\overline{AI}}$, is introduced and analyzed in details over two major sources, one in Africa the other in Afghanistan. Then, the relation is applied to 11 other major sources over different continents. The results are discussed before concluding.

2. Data Description

2.1. Meteorological Data

[4] The meteorological data used in our analysis are provided by the Goddard Earth Observatory System-Data Assimilation System (GEOS-DAS) analysis on a 2.5° longitude by 2° latitude horizontal resolution. This data set provides observed meteorological fields on a regular grid since February 1981 with surface fields archived every 3 hours [*Schubert et al.*, 1993]. The meteorological fields used in our analysis are the surface pressure (p_s), the friction velocity (u_*), the planetary boundary layer depth (h_{PBL}), the soil moisture (w), and the precipitation ($Prec$). The surface stress velocity, or the friction velocity, is defined in GEOS-DAS as the wind speed at the surface layer top impeded by the surface drag:

$$u_* = C_u W_s \tag{1}$$

where C_u is the nondimensional surface drag coefficient, and W_s is the surface wind speed, evaluated at 1 meter above ground. The surface drag coefficient is obtained from the similarity functions for the stability dependent flux profile relationships. The surface wind speed, W_s, is calculated for the last internal turbulence time step from the analyzed wind speed at the first model level above the Earth's surface. The planetary boundary layer depth, h_{PBL}, is diagnosed as the level at which the turbulent kinetic energy is reduced to a tenth of its surface value. It has been converted from depth (mb) to an altitude (m) above the Earth's surface using the hydrostatic law. The surface soil moisture, w, is calculated from a prognostic equation which includes the precipitation, surface temperature, and solar radiation [*Schubert et al.*, 1993].

[5] For this study, the fields have been extracted from 1981 to 1990 to obtain a period long enough to study the interannual variability, and to avoid different TOMS instruments and GEOS-DAS versions. The meteorological fields are linearly interpolated in space from the GEOS-DAS grid to the dust sources coordinates estimated by *Prospero et al.* [2002], and in time to local noon which corresponds approximately to the TOMS passing time.

2.2. TOMS Measurements

[6] The TOMS instrument on board the satellite Nimbus 7 measured aerosol backscattering radiances at 340 and 380 nm from November 1978 until May 1993. In this study, we use the data from the period 1981–1990. These measurements cover the Earth daily with a 50 km resolution at satellite footprint. The local passing time is about 11:30 am. By taking the difference between the measured and calculated radiances for a purely molecular atmosphere, *Herman et al.* [1997] defined the TOMS Aerosol Index (TOMS AI) as follow

$$\mathrm{AI} = -100\left\{\log_{10}\left(\frac{I^m_{340}}{I^m_{380}}\right) - \log_{10}\left(\frac{I^c_{340}}{I^c_{380}}\right)\right\}, \tag{2}$$

where I^m is the backscattering radiance measured by TOMS at the given wavelength and I^c is the radiance calculated using a radiative transfer model for a pure Rayleigh atmosphere. In this study, we use the version 7 uniformly grid level 3 data product (1.25° longitude and 1° latitude). The TOMS AI is a qualitative indicator of the presence of UV absorbing aerosols. An inversion procedure that retrieves aerosol properties from the TOMS radiances has been developed by *Torres et al.* [1998]. They have shown that for absorbing aerosols, like dust particles, the optical thickness can be derived from the TOMS AI knowing the values of single scattering albedo, the altitude of the aerosol layer, and the surface pressure, and assuming a refractive index. In this study, the real and imaginary parts of the refractive index correspond to the values derived by *Sinyuk et al.* [2003]. The major drawback of the method is the possibility of subpixel clouds contamination. *Torres et al.* [1998] proposed to use a threshold of 15% observed reflectance to eliminate most clouds contamination. All data have been screened using a maximum reflectance of 13%.

3. Empirical Relation, $\overline{AI}$

[7] The idea here is to express explicitly TOMS AI as a function of the optical thickness, single scattering albedo, altitude of the dust layer, and surface pressure. There is no analytical solution of equation 2 expressing these variables. Our method consists of finding empirically the best fit to the TOMS AI calculated with a radiative transfer code for a set of values of the 4 variables. The radiative transfer calculation is described in detail by *Torres et al.* [2002]. Unfortunately,

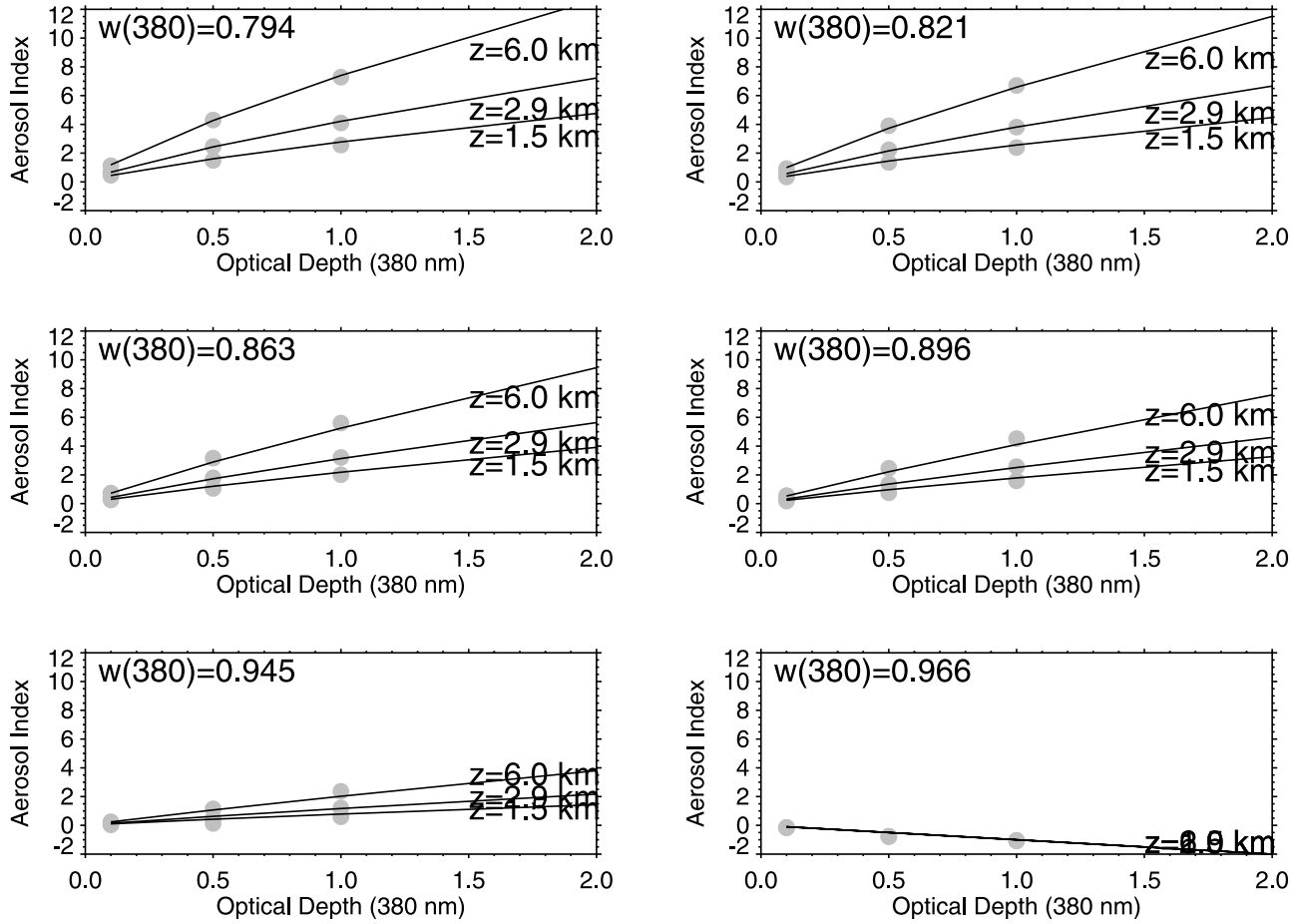

Figure 1. Comparison between $\overline{AI}$ (black lines) and AI calculated from radiative calculation (gray dots) for 6 values of ω_{380} (one for each panel), 3 altitudes (1.5, 2.9 and 6 km), and 3 optical depth at 380 nm (0.1, 0.5, and 1).

our method does not provide a unique solution. Many different functions could be found which fits the TOMS aerosol index. So, we based our empirical function on previous analyses. Sensitivity analyses by *Torres et al.* [1998] and *Hsu et al.* [1999] have shown that the TOMS aerosol index is proportional to the dust plume altitude. They have also shown that the dependency on the altitude increases as the single scattering albedo decreases, with no dependency for nonabsorbing aerosol. This means that the linear dependency on the altitude is scaled by the single scattering coalbedo. *Hsu et al.* [1999] have shown that the TOMS AI and the optical thickness measured by ground-based sun-photometers are linearly correlated. By fitting *Torres et al.* [1998] results, we found that the TOMS aerosol index is proportional to the optical thickness at the power of the single scattering albedo. For weakly absorbing aerosol, the dependency is almost linear but as the absorption increases (or the single scattering albedo decreases) the departure from linearity is more significant, especially at high optical thickness ($\sim$2). But this departure from linearity is relatively weak because dust single scattering albedo is around 0.85 in the nUV [*Colarco et al.*, 2002]. Based on these dependencies, we have established an empirical aerosol index, $\overline{AI}$, as a function of the surface pressure (p_s), the single scattering albedo at 380 nm (ω_{380}), the optical thickness at 380 nm(τ_{380}), and the altitude of the aerosol layer (h):

$$\overline{AI} = (1 - 0.2\log(p_s))[1.25 + 5(1 - \omega_{380})h](\tau_{380})^{\omega_{380}} \qquad (3)$$

where $0.6 \leq p_s \leq 1$ atm, and $0.75 \leq \omega_{380} \leq 0.95$. Beyond $\omega_{380} = 0.95$, $\overline{AI} = -\tau_{380}$.

[8] This formula gives a first order approximation of the TOMS AI and should be replaced by the exact radiative calculations if one wants to determine the exact optical properties.

[9] Figure 1 shows the comparison between the values of AI and $\overline{AI}$, and their relative differences. The comparison is shown for the set of values of the surface pressure (p_s = 1 atm), single scattering albedo at 380 nm (ω_{380} = 0.794, 0.821, 0.863, 0.896, 0.945, and 0.966), altitude of aerosol layer (h = 1.5, 3, and 6 km) and optical thickness at 380 nm (τ_{380} = 0.1, 0.5, 1, and 2.5). The maximum relative error is around 30%, but in general the error is between 1 and 10%.

3.1. Sensitivity and Error Analyses

[10] In this section, the sensitivity of $\overline{AI}$ to the four variables (p_s, h, ω_{380}, and τ_{380}) are analyzed, as well as the errors associated with the relation (3).

[11] A variation Δ of $\overline{AI}$ can be calculated by taking the partial derivatives ∂ of $\overline{AI}$ relative to p_s, h, ω_{380}, and τ_{380}, and its is given by

$$\Delta\overline{AI} = \left(\frac{\partial\overline{AI}}{\partial p_s}\right)\Delta p_s + \left(\frac{\partial\overline{AI}}{\partial h}\right)\Delta h + \left(\frac{\partial\overline{AI}}{\partial \omega_{380}}\right)\Delta\omega_{380} + \left(\frac{\partial\overline{AI}}{\partial \tau_{380}}\right)\Delta\tau_{380} \quad (4)$$

where the partial derivatives correspond to the terms of the Jacobian and represent the sensitivity of $\overline{AI}$ to one variable, the others being fixed. Considering Δp_s, Δh, $\Delta\omega_{380}$, and $\Delta\tau_{380}$, the errors associated with p_s, h, ω_{380}, and τ_{380}, respectively, it is possible with the relation (4) to estimate the errors on $\overline{AI}$. Such estimations are important for model validation using the TOMS aerosol index. The relative error of $\overline{AI}$ due to each four variables are given by

$$\frac{\Delta\overline{AI}}{\overline{AI}} = \frac{1}{\log_{10} p_s - 5}\frac{\Delta p_s}{p_s} + \frac{1}{1 + \frac{1.25}{5(1-\omega_{380})h}}\frac{\Delta h}{h} + \left(\frac{-5h\omega_{380}}{1.25 + 5(1-\omega_{380})h}\omega_{380}\log_{10}\omega_{380}\right)\frac{\Delta\omega_{380}}{\omega_{380}} + \omega_{380}\frac{\Delta\tau_{380}}{\tau_{380}} \quad (5)$$

The 4 terms of the right hand side represent the elements of the Jacobian matrix: J_{ps}, J_h, J_ω, and J_τ. From this equation, it appears that the relative errors are all independent on τ_{380} and with a good approximation on p_s. Except for J_{ps}, all terms depend on ω_{380}. The dependency is different between terms: J_h decreases with increasing ω_{380}, while J_τ increases with increasing ω_{380}. Both the $\Delta\omega_{380}$ and Δh terms are proportional to h. Figure 2 shows the variability of the jacobian terms, the relative error of $\overline{AI}$ associated with Δp_s = 0.1 atm, Δh = 1 km, $\Delta\omega_{380}$ = 0.05 and $\Delta\tau_{380}$ = 0.2, and the departure of the four variables associated with an error $\Delta AI = 0.5$. The variability is shown as a function of two variables with fixed values for the two others. We have chosen typical values for p_s = 1 atm, h = 3 km, τ_{380} = 0.5, and ω_{380} = 0.85. The jacobian terms J_{ps} and J_w, associated with p_s and ω_{380} are negative, while J_h and J_τ are positive. In other words, $\overline{AI}$ will increase with increasing h and τ_{380} and decrease with increasing p_s and ω_{380}. The sensitivity of $\overline{AI}$ to h increases as τ_{380} increases and weakly decreases with increasing ω_{380}. For optical thickness lower than 0.2, the sensitivity of $\overline{AI}$ to ω_{380} is independent of height, but is highly sensitive for $\tau_{380} > 0.5$. The sensitivity of $\overline{AI}$ to τ is mostly dependent on h. The panels in the second column in Figure 2 provide the estimated error when calculating $\overline{AI}$ with p_s, h, ω_{380}, and τ_{380} knowing their errors, 0.1 atm, 1 km, 0.05, and 0.2. These 4 estimated errors are quite large and should be considered as an upper limit. The corresponding error of $\overline{AI}$ due to Δp_s is only 2% and is negligible. The errors associated with h and τ are of the same order, around 25% and 35%, respectively. The error associated with $\Delta\omega$ is negligible near the surface but is around 25% at 5 km altitude. This means that an estimated value of Δ_ω = 0.85 could be used for most cases, and it is preferable to obtain higher precision for τ_{380} than for h, although the sensitivity of $\overline{AI}$ on h is higher than on τ particularly for strongly absorbing dust particles. As can be seen from the right panels in Figure 2, the worst choice, when retrieving physical quantities from $\overline{AI}$, would be to determine the surface pressure, which is obvious, followed by the single scattering albedo for low optical thickness or near the ground. Deriving the plume altitude will have acceptable error for optical thickness larger than 0.5. The best choice is to derive τ_{380}, although it can have large error for aerosol layer lower than 1 km altitude.

3.2. Case of Other Absorbing Aerosols

[12] The relation (2) has been established for dust aerosol assuming values of absorption in the nUV derived by *Sinyuk et al.* [2003]. For dust particles, the absorption increases with decreasing wavelength, but for carbonaceous aerosols the absorption is spectrally flat [*Dubovik et al.*, 2002]. Consequently the parameters in relation (3) should be modified in case of carbonaceous aerosols.

4. First Application: Validation of Simulated Dust Distributions

[13] Dust distribution has been simulated for several years using the Global Ozone Chemistry Aerosol Radiation and Transport (GOCART) model. The GOCART model simulates the distribution of dust, sulfate, carbonaceous (organic and black carbon), and sea-salt aerosols. Each model component has been described in detail elsewhere [*Chin et al.*, 2000; *Ginoux et al.*, 2001, 2003].

[14] Briefly, the GOCART model is a global scale model driven by the Goddard Earth Observing System Data Assimilation System (GEOS DAS). It has a horizontal resolution of 2° latitude by 2.5° longitude and 20 to 40 vertical layers (vertical resolution depends on the version of GEOS DAS). The model contains the following modules in dust simulation: sources based on topographic depressions with bare soil; advection, which is computed by a flux-form semi-Lagrangian method; boundary layer turbulent mixing, which uses a second order closure scheme; moist convection, which is calculated using archived cloud mass flux fields; dry deposition at the surface by eddies; wet deposition, which accounts for the scavenging in convective updrafts and rainout/washout in large-scale precipitation.

[15] An interesting case study is the evolution of a Sahara dust plume which evolves in complex patterns for several days over the North Atlantic in March 1988. The TOMS AI index is particularly useful to assess the possibility for models to simulate its formation and capture its complex patterns for several days. The methodology consists to first calculate the optical thickness at 380 nm from the relation:

$$\tau_{380} = \sum_{k=1}^{7}\tau_k = \sum_{k=1}^{7}\frac{3}{4}\frac{Q_k\alpha_k M_i}{r_k\rho_{pi}} \quad i = 1 \text{ for } k \le 4 \text{ and } i = k-3 \text{ for } k > 4 \quad (6)$$

where τ_k is the optical thickness at 380 nm for 7 bins k, Q_k is the extinction efficiency at 380 nm, M_i is the column mass loading of bin i of the 4 transported size bins, α_k is the fraction of each 7 subbins, r_k is the effective radius, and ρ_{pi} is the mass density of the size class i. The values of $Q_k(380\ nm)$ are calculated using Mie theory and using the real and imaginary parts of the refractive index derived by

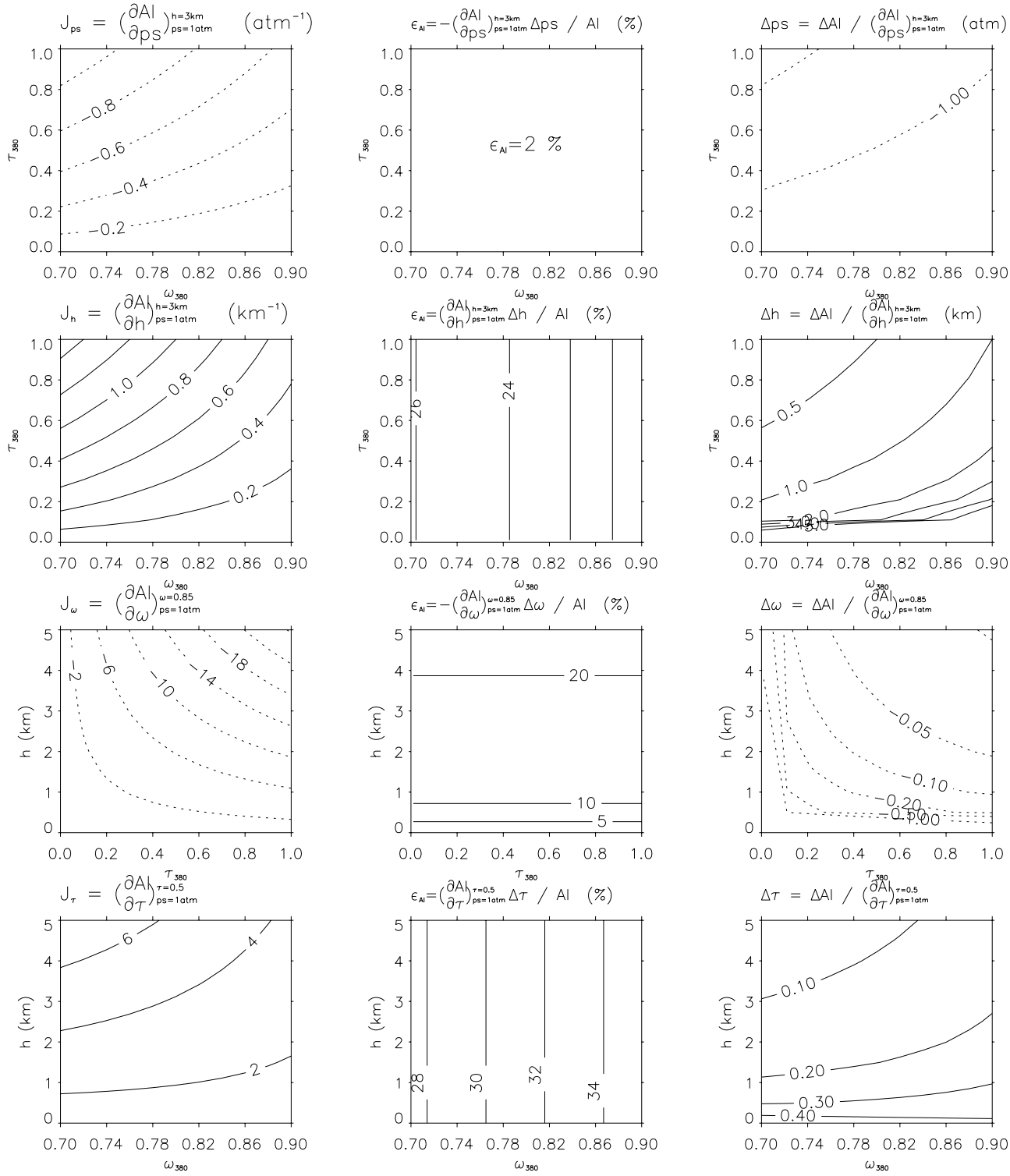

Figure 2. Sensitivity (left panels), relative errors (middle panels) and error associated with a departure ΔAI = 0.5 (right panels) of the empirical function $\overline{AI}$ as a function of the surface pressure p_s (upper panels), the altitude of the plume h (second row), the single scattering albedo ω_{380} (third row), and the optical thickness τ_{380} when varying or fixing to typical values (p_s = 1 atm, h = 3 km, ω_{380} = 0.85, τ_{380} = 0.5) the other 3 variables.

Colarco et al. [2002]. Second, the single scattering albedo at 380 nm (ω_{380}) is calculated by the relation

$$\omega_{380} = \frac{\sum_{k=1}^{7} \omega_k \tau_k}{\tau_{380}} \quad (7)$$

where ω_k is the single scattering albedo which is calculated using Mie theory for which the particle effective radius r_k and the refractive index Q_k are provided. The values of r_k, α_k, Q_k, ρ_{pi}, and ω_k are given in Table 1. Third, the centroid of mass Z is calculated by the formula

$$Z = \frac{\sum_{j=1}^{nlev} \left(\sum_{i=1}^{4} m_{i,j} \right) z_j}{\sum_{i=1}^{4} M_i} \quad (8)$$

where z_j is the altitude above ground at level j among the *nlev* model levels, $m_{i,j}$ is the mass concentration of size class i at level j, and M_i is the mass column.

[16] Figure 3 shows the values of the optical thickness, single scattering albedo (ω_{380}), and the centroid of mass (Z) for a dust plume emitted from Sahara and evolving over the North Atlantic in March 1988. Around the 27 March 1988, a dust plume was produced from Sahara and transported by the Azores high towards Europe. Two days later, the plume is separating in two branches when West and the other East. The West branch formed two days later half a circle over most of the North Atlantic.

[17] With τ_{380}, ω_{380}, Z, the empirical function $\overline{AI}$ can be calculated from 3 assuming a constant surface pressure. Figure 4 shows the comparison between the observed and calculated aerosol index for the March 1988 dust plume. For comparison the exact calculation of TOMS AI using GOCART output, as described by *Ginoux et al.* [2003], is also shown. From Figure 2, it appears that $\overline{AI}$ is more sensitive to τ_{380} than with the radiative calculation: higher $\overline{AI}$ over sources with high τ_{380} and lower $\overline{AI}$ in the remote regions. But overall, the $\overline{AI}$ and the radiative calculation give comparable results.

5. Second Application: Dust Sources Characterization

5.1. Second Empirical Relation, $\overline{\overline{AI}}$

[18] In this section, we analyze the possibility to retrieve some characteristics of dust sources from the TOMS AI. The sensitivity and error analyses of $\overline{AI}$ have shown that large errors occur when deriving quantities near the ground, in particular the single scattering albedo. It would then seem ambiguous to still attempt to use $\overline{AI}$ to characterize dust sources. The motivations are practical and intellectual. In the absence of in situ measurements the only possibility to improve our understanding of source characteristics is with satellite data. Also, the presented methodology could possibly be applied to satellite radiances which are less sensitive to the altitude, as in the visible.

[19] The methodology presented in this section consists to substitute the optical thickness and altitude of the plume with meteorological variables such that the variables in relation (3) are related to surface characteristics.

5.1.1. Elevation of the Aerosol Layer

[20] *Karyampudi and Carlson* [1988] and *Karyampudi et al.* [1999] developed a dust plume conceptual model for North Africa, and showed that the formation of major dust outbreaks corresponds generally to wind acceleration induced by strong surface pressure gradient usually associated with the approach of surface cyclone. The winds converging towards the intense heat low over arid regions pick up large amount of dust particles from loose topsoil and generate dust clouds. In a theoretical study focusing on dust vertical transport, *Bounoua and Krishnamurti* [1991] have shown that, during dust outbreaks, upward motion prevails in the mixed layer while there is a downward motion aloft. This two-cell circulation creates an anticyclonic outflow at the top of the mixed layer. Assuming here that such mechanism is at the origin of most dust plumes, the dust elevation h in equation (3) can be replaced by the planetary boundary layer height h_{PBL}

$$h = h_{PBL} \quad (9)$$

[21] Assuming a well mixed atmosphere, the optical thickness can be expressed by $\tau_{380} = B_{380} m$, where B_{380} is the specific extinction cross section at 380 nm and m is the mass column per surface area. *Kinne et al.* [2003] have estimated that B_{550} values range from 0.5 to 2 $m^2\ g^{-1}$ based on the results from several global models, including GOCART. The extinction efficiency is a function of the particle size and wavelength. The dust mass column is the integral of dust mass concentration over the source. The dust concentration can be calculated by the continuity equation which expresses that mass variation in space and time is due to transport by wind advection, cloud convection and turbulent diffusion, and removal. The mass concentration over the surface of a dust source will be mostly controlled by the rates of emission (Φ_{up}) and loss rate (L):

$$\frac{\partial m}{\partial t} \sim \Phi_{up} - Lm \quad (10)$$

In this equation we have neglected the wind advection, cloud convection and horizontal diffusion. At steady state, $m = \frac{\Phi_{up}}{L}$. We consider only dry conditions such that the loss rate is only due to dry deposition by settling and turbulence. The loss rate L is formulated by a deposition velocity v_d at a fixed level h_{dep}.

[22] Dust is uplifted into the atmosphere by saltation bombardment of coarse particles. A typical saltation model has been formulated, suggesting that for soils with uniform particle size, the horizontal flux of large particles Q, is given by

$$Q = \begin{cases} \frac{C\rho}{g} u_*^3 \left(1 - \left(\frac{u_t}{u_*}\right)^2\right) & u_* > u_t \\ 0 & \text{otherwise} \end{cases}, \quad (11)$$

Table 1. Properties of Dust Particles Used to Calculate an Aerosol Index[a]

k	r_k, μm	i	α_k	ρ_p, kg m^{-3}	Q_k, 380 nm	ω_k, 380 nm
1	0.14	1	0.01	2650	0.732	0.962
2	0.24	1	0.08	2650	0.276	0.976
3	0.45	1	0.25	2650	3.975	0.968
4	0.8	1	0.65	2650	2.427	0.905
5	1.5	2	1	2650	2.354	0.861
6	2.5	3	1	2650	2.228	0.798
7	4.5	4	1	2650	2.182	0.725

[a]Effective radius (r_k) of the subbin k of the 4 transported bins (i), size fraction of the subbin (α_k), mass density (ρ_p), extinction efficiency at 380 nm (Q_k), and single scattering albedo at 380 nm (ω_k).

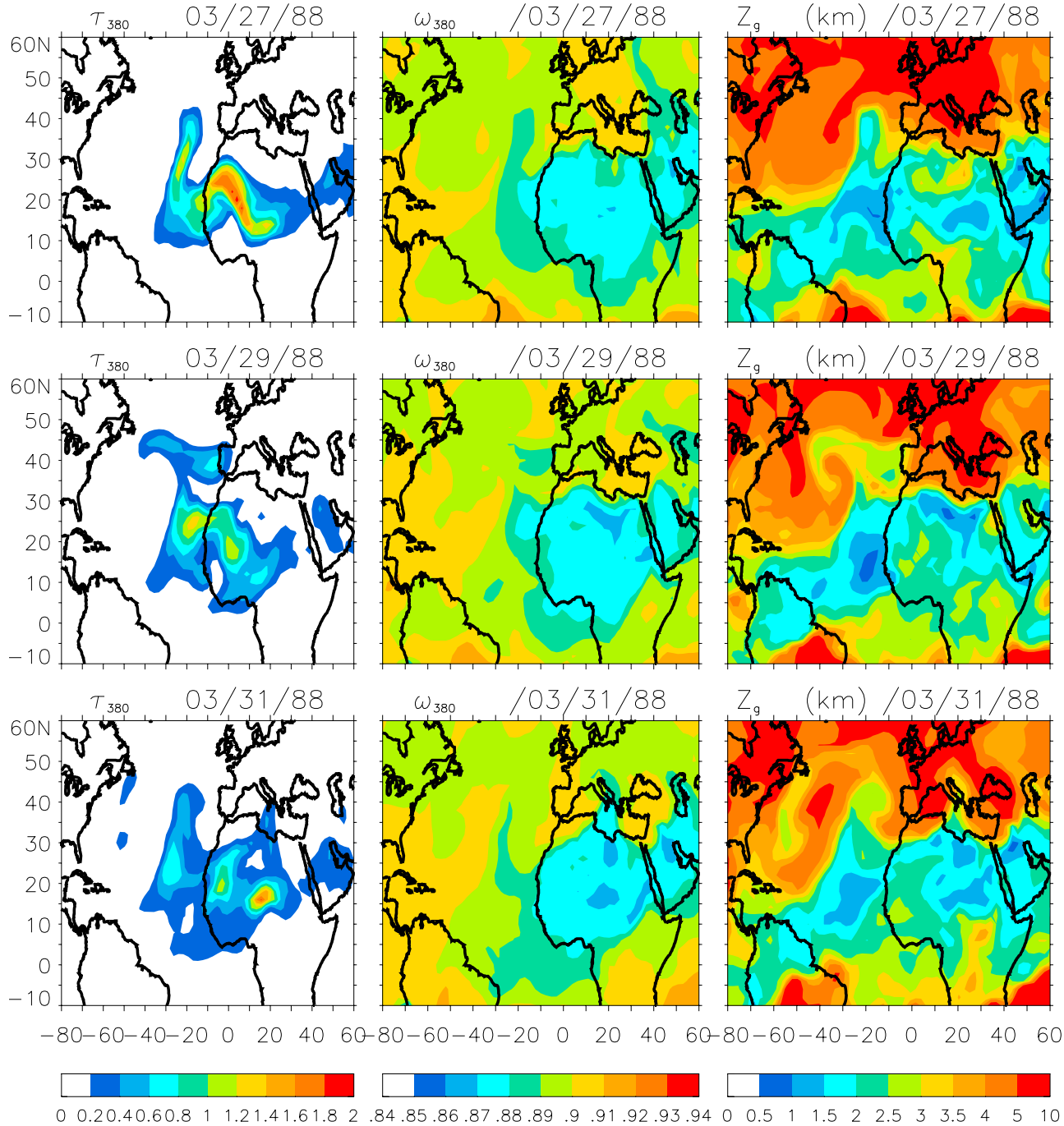

Figure 3. Calculated values of the optical thickness at 380 nm (left panels), single scattering albedo at 380 nm (middle panels), and centroid of mass (right panels) in units of km, for a Saharan dust plume evolving on the 27 (first row), 29 (second row), and 31 (third row) March 1988.

where C is a constant of order unity, ρ is the air density, g is the acceleration of gravity, u_* is the friction velocity, and u_t is the threshold velocity of wind erosion. The threshold velocity, u_t, is a function of the interparticle forces which depends on the particle size and the soil moisture. The threshold velocity increases rapidly for moist conditions [*Fécan et al.*, 1999]. We consider, in this study, only dry conditions and the meteorological fields are extracted when the soil moisture is less than 20%. The vertical dust flux, Φ_{up}, is estimated from the horizontal flux Q, using an efficiency factor α: $\Phi_{up} = \alpha Q$. The factor α is a function of the parent soil texture [*Marticorena and Bergametti*, 1995].

[23] The dry deposition at the surface includes the gravitational settling and the turbulent transfer to the surface. These two terms depend on the particle size and the friction velocity. *Gillies et al.* [1996] have monitored intense dust plumes over Mali. Their data showed that the grain-size distribution of a fallout sample covered a wide range of particles sizes (up to >70 μm) with a mean particle size of 16.8 μm. To eliminate the dependency on size distribution,

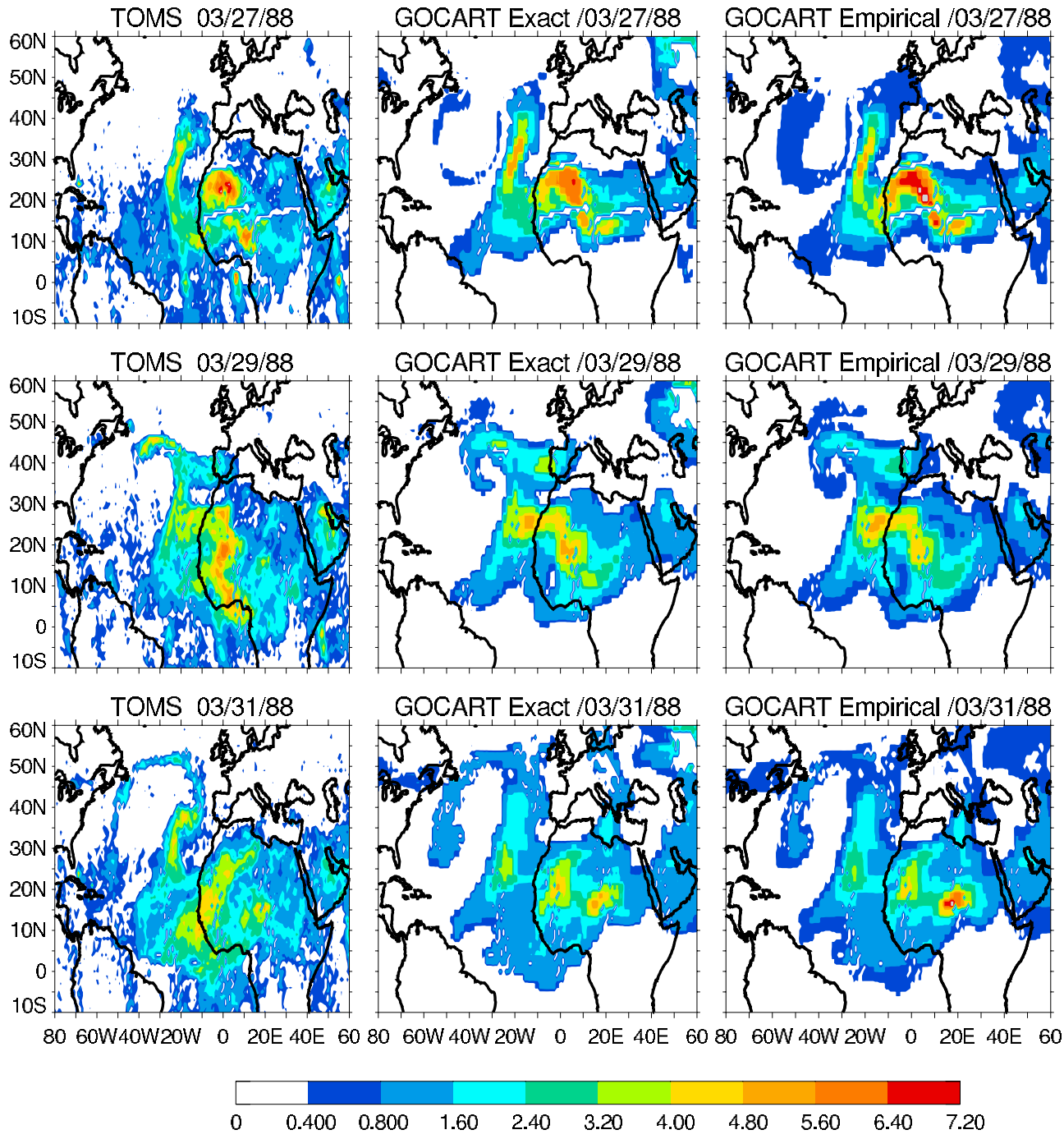

Figure 4. TOMS Aerosol Index (left panels), calculated index with exact radiative calculation (middle panels), and $\overline{AI}$ (right panels) for a Saharan dust plume evolving on the 27 (first row), 29 (second row), and 31 (third row) March 1988.

we assume a mean particle size of 17 μm for every dust sources. The detail method of linearization of v_d is provided in Appendix A, and the deposition velocity for 17 μm particles can be approximated by

$$v_{d17} \sim 3u_*^2, \tag{12}$$

in units of m s^{-1}.

[24] After substituting in 3, h by h_{PBL}, τ_{380} by $\frac{\alpha\Phi_{up}}{v_d h_{dep}}$ with Φ_{up} given by expression 11 and v_d by the approximation 12, the TOMS aerosol index can be replaced by an empirical index, $\overline{\overline{AI}}$, given by

$$\overline{\overline{AI}} = A(1 - 0.2\log(p_s)) \times (1.25 + 5(1 - \omega_{380})h_{PBL}) \times \left(u_*\left(1 - \left(\frac{u_t}{u_*}\right)^2\right)\right)^{\omega_{380}} \tag{13}$$

where A is the dimensional constant of proportionality and is a function of α, h_{dep}, B_{380}, and $\frac{C_p}{g}$.

Table 2. Dust Source Characteristics[a]

	Source	Longitude	Latitude	Altitude, m	Diurnal, LT	N_d	R_d	ω_{380}	N_m	R_m	A	Δu_*, %	Δh_{PBL}, %
1	Tunisia	7.5E	33N	120	0–3pm	1876	0.5	0.85	89	0.86	2.5	6	19
2	Libya	20E	26N	210	0–3pm	810	0.46	0.85	45	0.85	2.3	7	11
3	Mauritania	6.5W	25.5N	180	0–3pm	2088	0.3	0.8	115	0.71	3.5	5	35
4	Mali	0	22N	240	9–12am	1747	0.42	0.95	112	0.77	3.8	5	55
5	Bodele	17E	17N	240	9–12am	2582	0.31	0.85	110	0.6	1.5	9	18
6	Sudan	29E	17N	460	9–12am	2465	0.55	0.75	107	0.88	1	5	13
7	Oman	55.5E	19N	150	9–12am	2777	0.59	0.75	117	0.88	1	6	7
8	Kuwait	46.5E	29.5N	240	0–3pm	2361	0.65	0.75	111	0.88	0.5	7	12
9	Aral Sea	61.5E	43.5N	90	0–3pm	1479	0.4	0.75	86	0.81	0.35	10	13
10	Afghanistan	61.5E	30N	400	3–6pm	2023	0.67	0.75	110	0.9	0.7	8	10
11	Taklamakan	83E	39N	910	3–6am	1357	0.34	0.75	97	0.72	0.7	7	12
12	Gobi	105E	40.5N	1220	9–12am	354	0.23	0.9	89	0.42	1.3	9	50
13	Lake Eyre	138E	25S	150	0–3pm	1098	0.18	0.95	110	0.5	1.6	7	32

[a]Number, location (region, longitude, latitude and altitude), local time period of most frequent surface winds >0.4 m s^{-1} (diurnal), total number of screened daily values (N_d), correlation coefficient between daily $\overline{AI}$ and TOMS AI (R_d), single scattering albedo at 380 nm (ω_{380}), total number of months with valid data (N_m), correlation coefficient between monthly $\overline{AI}$ and TOMS AI (R_m), slope of the regression line between $\overline{AI}$ and TOMS AI (A), mean relative difference of monthly friction velocity (Δu_*) and planetary boundary layer height (Δh_{PBL}) over 10 years.

[25] The different assumptions made to establish the empirical expression 13 limit considerably its validity to unstable dry atmospheric conditions with no significant import from other sources and export by horizontal transport, no accumulation of airborne particles, and dry conditions. The errors associated with horizontal mixing are expected to be quite large especially as the resolution of the satellite and meteorological fields gridded data is coarse and the TOMS passing time does not necessarily correspond to the diurnal maximum of dust emission.

5.1.2. Selected Dust Sources

[26] Among the numerous sources identified by *Prospero et al.* [2002], we limit our study to 13 sources located in different continents. Table 2 gives the approximate location and altitude of the 13 sources. The sensitivity study and error analysis are performed over the sources in Afghanistan and the Bodele depression.

5.1.3. Error Associated With the Resolution of the Data Sets

[27] We have seen in section 3.1 that the errors associated with the relation $\overline{AI}$ increase as the dust layer comes close to the ground. Another important source of error is due to the coarse resolution of the data sets. Figure 5 upper-left panel shows a large dust storm viewed by the Sea-viewing Wide Field-of-view Sensor (SeaWIFS) at the border between Iran, Pakistan and Afghanistan. The various shades of color reflect a varied landscape containing expanses of flat open desert, dry lake beds, dune fields, and mountain ranges. The large orange-brown stingray shaped on the upper right is the sandy desert Rigestan. The dark brown splotches South of the Ragestan is the Pakistan's Chagai Hills, and West is the Iranian Seistan mountains. The light brown spots in the upper part between 61 and 62 degrees longitude East is the Daryacheh-ye-Hamum dry lake which has been identified as a major dust source by *Prospero et al.* [2002]. The dust plume is clearly originating from this dry lake. This exemplifies the importance of dry lakes in topographic depression relative to sand deserts to produce large dust plumes. The fact that the dust plume is deflected to the East down the Helmand valley by the Chagai Hills indicates that the plume is for that day about 2 km altitude. Figure 3 lower-left panel shows the TOMS aerosol index as it was derived over the same region, on the same day and time (March 18, 2001, local noon). The isovalues of TOMS AI have been plotted over the topography. Figure 3 upper-right panel shows a MODIS photo of dust plumes emitted in March 2002 from the Bodele depression. The depression is located South of the Tibesti mountains visible in the upper right corner, and North-East of the Lake Chad (dark blue in the lower left corner). A black line indicates the border between Chad and Niger. A difference with Figure 3a is the multiplicity of plumes emitted from different locations of the Bodele depression. Figure 3d shows the corresponding Aerosol Index with the highest value just over the lowest point of the depression (dark green). The selected grid points and grid cells of TOMS data (in red) and the GEOS DAS meteorological fields (in blue) are shown on Figure 3 lower-right panel. Both points are slightly off the maximum of the TOMS aerosol index which peaks at 4 over the depression.

[28] The SeaWIFS and MODIS pictures indicate that the coverage of dust sources varies considerably between regions. In Afghanistan the source area is limited to a few tenth of a degree while TOMS data are provided on a 1 by 1.25 resolution grid and the GEOS DAS meteorological fields are given on a 2 by 2.5 grid. To give an idea of the different resolutions, we have over plotted on Figure 3 lower panels the center (dot) and contour of the cell (square) of TOMS data (in red) and GEOS DAS fields (in blue) used to characterize these two sources. Over Afghanistan, TOMS grid cell envelopes a much larger area than the actual sources, while over the Bodele depression several sources are just outside the grid cell. Therefore, the constant of proportionality A in relation (13) will depend on the fraction of the TOMS grid cell covered by the source. In the case of the Bodele depression, the contamination from the surrounding sources will bias comparison between TOMS AI and $\overline{AI}$. The Afghanistan source is surrounded by mountains and the contribution from other sources should be limited. This is apparent on the right of Figure 3 lower-left panel, where a dust plume from India is blocked on the East by the mountain ridge. Other sources of error are the quality of analyzed wind fields over deserts, as discussed by *Shay-El et al.* [1999], and the coarse resolution of the meteorological fields. With a 2° by 2.5° grid, the effects of subscale variability of terrain can be significant, as for example the

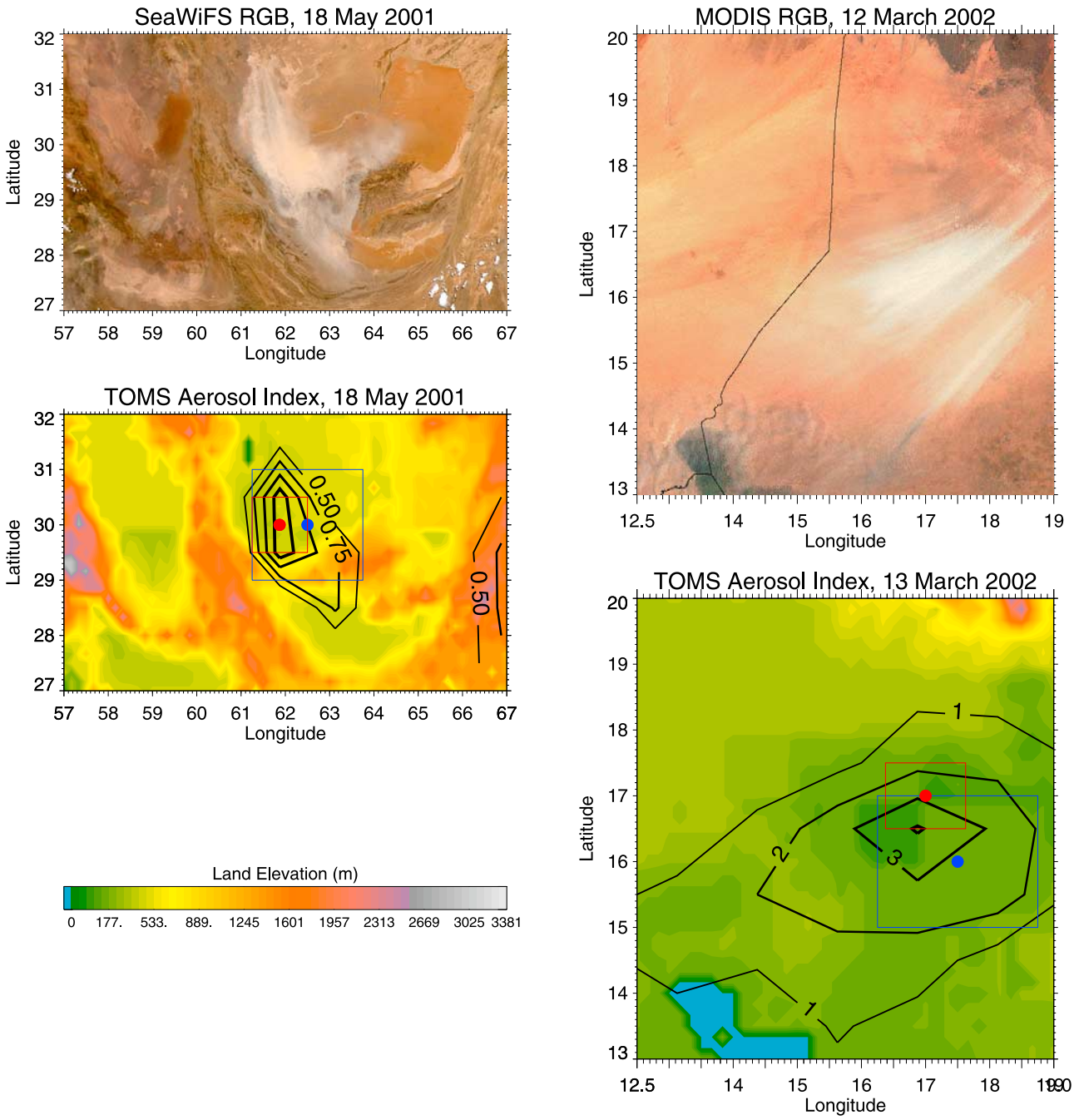

Figure 5. Dust plumes from Afghanistan observed by SeaWiFS (upper left panel) and TOMS (lower left panel) on the 18th May 2001 and Bodele depression observed by MODIS (upper right panel) on the 12th March and TOMS (lower right panel) on the 13th March 2002. The upper panels are composite of red, green, and blue channels. The lower panels show land elevation in the background, the TOMS Aerosol Index isovalues, the grid points and cells of TOMS and GEOS DAS data.

acceleration of winds over ridges. Such phenomenon could be at the origin of the source line long by almost 100 km in the middle of the picture on Figure 3 upper-right panel.

5.1.4. TOMS Satellite Local Passing Time

[29] The TOMS satellite NIMBUS-7 is orbiting with a local passing time around 11:30 am. The variability is less than half an hour for the entire Nimbus-7 lifespan. To establish the empirical relation (13), it is assumed that the observed dust plume is instantaneously emitted from the ground. If most dust plumes are generated before TOMS passing time, the observed plume will be aged and partially depleted from its original mass. On the other hand, if most dust plumes are generated after TOMS observation, the source will seem less active than it is. In this section, we will examine the diurnal variation of the surface wind speed as a proxy for source activity.

[30] Figure 6 shows the diurnal frequency of the three hours average friction velocity u_* greater than 0.4, 0.6 and 0.8 m s^{-1}. The most frequent wind speed is between 3 and 6 pm, for all three threshold speeds. Before noon, high

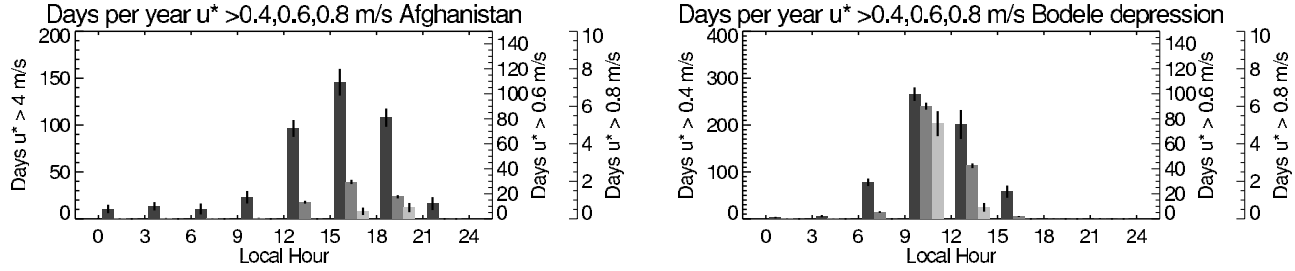

Figure 6. Diurnal variation of the number of days per year (average over 10 years) the friction velocity u_* is greater than 0.4 (dark gray), 0.6 (medium gray), and 0.8 (light gray) ms^{-1} for Afghanistan (left panel) and Bodele depression (right panel).

surface wind speed is infrequent. This means that, statistically, TOMS satellite is slightly ahead of the maximum dust activity. It is interesting to see if this affects a seasonal analysis. By plotting the seasonal variation of the frequency of wind speed greater than 0.4 m s^{-1} during 9 am to noon, noon to 3 pm, and 3 to 6 pm, in Figure 7, we see that similar seasonal variation is obtained for the three periods. In other words, the seasonal variation of the Afghanistan source activity studied from TOMS data is representative, even though this source should appear more active. This is not always true for other sources. Table 2 summarizes in column 6 (Diurnal) the time of the most frequent surface wind speed greater than 0.4 m s^{-1} over 13 major dust sources. We can see that over the Sahara (region of Africa North of 20°N) the peak is early in the afternoon while over the Sahel (arid regions South of the Sahara) it is late in the morning, around TOMS passing time. It is thus possible that TOMS measurements underestimate Saharan dust at the sources.

5.2. Sensitivity Analysis

[31] The empirical Aerosol Index, $\overline{\overline{AI}}$, is a function of three meteorological fields (p_s, h_{PBL}, and u_*) and has three degrees of freedom (A, ω_{380} and u_t). The three meteorological fields are extracted at local noon when the TOMS observed reflectivity is less than 13% and the soil moisture, calculated by NASA GEOS DAS, is less than 20%. Table 2, column N_d, gives for 13 major dust sources the total number of screened values over ten years, from January 1981 to December 1990. By varying h_{PBL} and u_*, the correlation coefficient between the TOMS AI and the empirical $\overline{\overline{AI}}$ given by equation (13) is calculated. The maximum value of R correspond to the best estimation of ω_{380} and u_t. The slope of the regression line between AI and $\overline{\overline{AI}}$ provides the value of A. We let ω_{380} vary from 0.75 to 0.95 with an increment of 0.05, and u_t from 0 to 0.4 m s^{-1} with an increment of 0.1.

[32] Figure 8 shows the comparison between the daily TOMS AI and empirical $\overline{\overline{AI}}$ for Afghanistan and Bodele depression. The regression lines are draw in black. For the Bodele depression comparison (Figure 8b), most points are clustered around the line $\overline{\overline{AI}} = 0.5\ AI - 1$ (gray line), but a significant number of points are underpredicted by the relation (13). We suspect that all the points below the unity line are due to import of dust from the upstream dust sources. This exemplifies the difficulty to use $\overline{\overline{AI}}$ when there is significant contamination from other sources. For the Afghanistan source, the highest R value is 0.67 and corresponds to $u_t = 0$ m s^{-1} and $\omega_{380} = 0.75$. The correlation coefficient is very high considering that it is calculated with more than 2000 points (column N_d in Table 2). The maximum value of R and the corresponding values of ω_{380} for the 13 sources are given in columns R_d and ω_{380} of Table 2, respectively.

5.2.1. Threshold Velocity

[33] For all sources, the highest correlation is obtained for near zero threshold velocity u_t. But the correlation coefficient does not vary significantly until 0.2 ms^{-1} after which it drops rapidly. Observations show a wide range of u_t values which are generally equal or higher than 0.25 m s^{-1} [e.g., *Gillete et al.*, 1980]. It is clear that all the errors associated with our method does not allow, unfortunately, to retrieve such parameter. But the problem can be addressed differently by defining a minimum threshold of AI which can be detected by TOMS. A value of 0.7 is generally used as a safe minimum threshold for detection of dust aerosol.

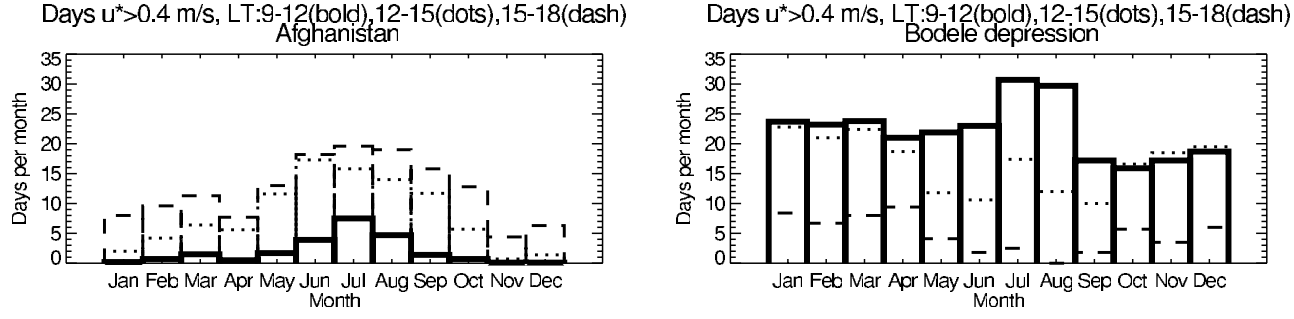

Figure 7. Seasonal variation of the number of days per month (average over 10 years) the friction velocity between 9 and 12 am (bold line), noon and 3 pm (dash line), and 3 and 6 pm (dash line) local time in Afghanistan (left panel) and Bodele depression (right panel) is greater than 0.4 ms^{-1}.

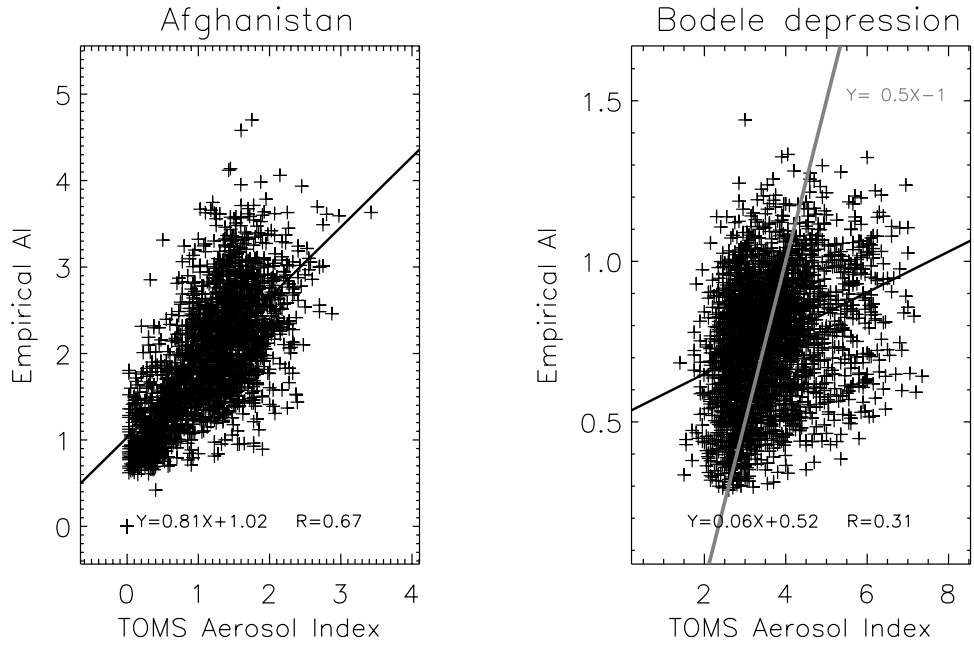

Figure 8. Comparison of the daily TOMS AI and $\overline{\overline{AI}}$ for 10 years over Afghanistan (left panel) and Bodele depression (right panel).

Figure 9 shows, for the sources in Afghanistan, Bodele depression and on the shore of the Lake Eyre, the seasonal variation of the frequencies of u_* greater than 0.2, 0.4, 0.6 and 0.8 ms^{-1}, and the frequency that the TOMS AI is greater than 0.7 (a low limit). For the Bodele depression, the frequency of detectable TOMS AI is greater than the frequency of low wind speed. This would mean that dust is generated by subscale process, like ridge acceleration or contamination from other sources. In the Lake Eyre region, the aerosols are detected by TOMS when the wind speed is greater than 0.6 m s^{-1} for all seasons. Such value is consistent with values derived in the Lake Eyre region by *Shao and Leslie* [1997]. In Afghanistan (Figure 9a) and for most dust sources (not shown), there is no seasonal correlation because of the strong altitude variation between seasons. The minimum seasonal frequency of TOMS AI > 0.7 is winter when the altitude is the lowest, and corresponds to winds greater or equal to a little less than

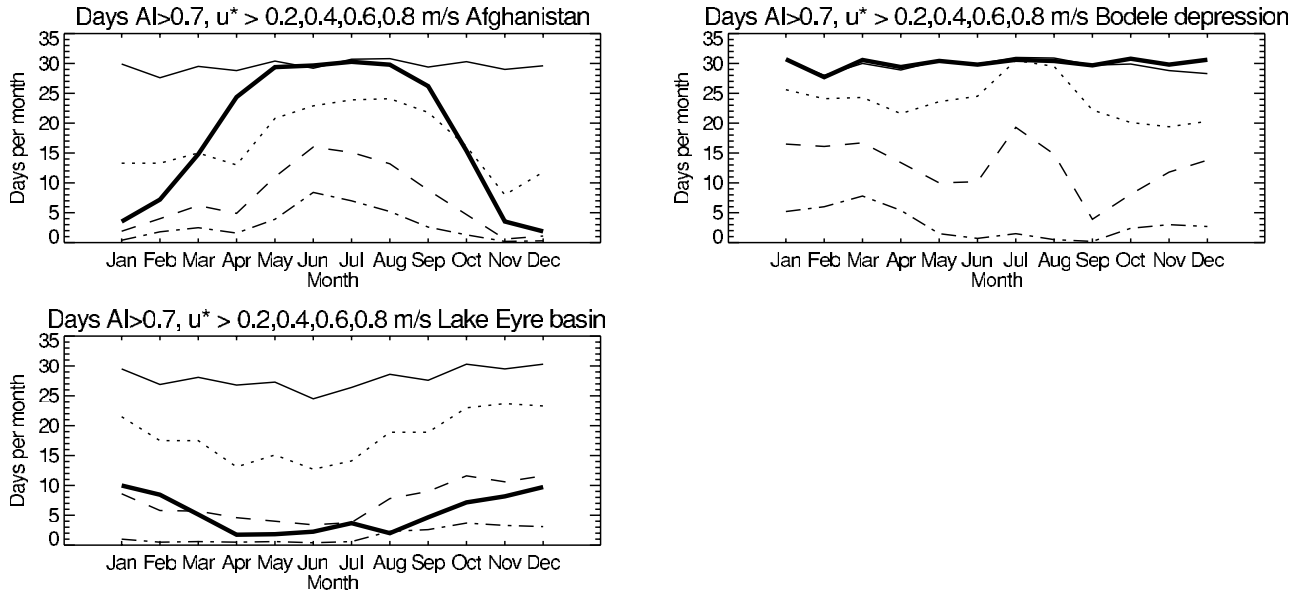

Figure 9. Seasonal variation of the number of days per month the TOMS AI is greater than 0.7 (bold line), and the friction velocity is greater than 0.2 (continuous line), 0.4 (dot line), 0.6 (dash line) and 0.8 (dash dot line) at local noon in Afghanistan (upper panel), Bodele depression (middle panel) and Lake Eyre basin (lower panel).

0.6 ms^{-1}. Such value is in the range of measured values elsewhere.

5.2.2. Single Scattering Albedo

[34] *Sokolik and Toon* [1999] have shown that the absorption properties of dust particles are a strong function of their mineralogy. The most and least absorbent minerals are respectively hematite and montmorillonite. Because the soil mineralogy varies between regions, we should expect spatial variation of the single scattering albedo. Our derived values of single scattering albedo for the 13 sources are given in Table 2. In Africa, the values range from 0.8 to 0.95 with the lowest value in east Sahel (Sudan) and the highest in Sahara over Mali. These values are significantly higher than the values reported by *Patterson et al.* [1977] which have been estimated to be too low, in the visible, by *Dubovik et al.* [2002]. *Colarco et al.* [2002] have determined the single scattering albedo of Saharan dust at 360 nm during summer 1997 from model simulations and TOMS radiances along the West coast of Africa. Their values range from 0.68 to 0.93 (their best value is close to 0.85) which are similar to the range of values we obtain for North Africa. Using TOMS radiances and sun-photometers data, *Sinyuk et al.* [2003] have retrieved the imaginary part of the refractive index of Sahara and Sahel dust which are comparable to *Colarco et al.* [2002]. They also found that Sahel dust is slightly more absorbing than Sahara dust which is consistent with our results. In Asia and Saudi Arabia Peninsula, all sources have a similarly low single scattering albedo, 0.75, except for the Gobi desert where it reaches 0.9. *Sokolik and Golitsyn* [1993] have derived a single scattering albedo at 400 nm around 0.77 from data collected during a 1989 field experiment in Tadzhikistan. In Australia, the dust is practically nonabsorbing with a single scattering albedo around 0.95. It is important to remind that even though these values correspond to published values, the errors on retrieved ω_{380} from relation (3) can be quite large below 1 km altitude and as the optical thickness decreases to ~0.2 (compare Figure 2).

5.2.3. Size Distribution

[35] In formula (13) we have assumed a mean diameter of 17 μm of falling particles, based on in situ measurement near the Mali dust source. The size distribution modifies strongly the deposition rate. As the particles get larger (>50 μm), gravitational settling dominates over the other dry deposition processes and the deposition rate is practically independent on u_*. In that case, $\overline{\overline{AI}}$ would depend at the cubic power of u_*. On the other hand, for submicron particles, the gravitational settling can be neglected and it is possible to show that the settling speed is proportional to u_*, and $\overline{\overline{AI}}$ depends on u_*^2. But we found that there is only a significant correlation between TOMS AI and $\overline{\overline{AI}}$, with a linear dependency on u_*. There is still a large range of possible values between 1 and 50 μm. By fitting the deposition velocity for 1 μm, 17 μm and 50 μm, and varying the diameter from 1 to 50 μm, the highest correlation coefficient are for diameter between 10 and 14 μm. This is slightly less than 17 μm but will not change our analysis.

5.2.4. Source Characteristics

[36] In relation (13) the constant of proportionality A is a function of the source characteristics, in particular α, and the relative dimension of the source compare to the TOMS grid cell. The values of A in Table 2 vary by a factor 10 between the lowest value near the Aral Sea (0.33) to the highest value over North Mali (3.8). *Marticorena and Bergametti* [1995] have shown that α is related to the soil clay content, but the variability of α for a given clay content is of the order of a factor 10. Such variability is comparable to the variability of A. It is unfortunately not possible to know the influence of the source size on A. The analysis of high resolution satellite data like MODIS or SeaWiFS could be very useful to determine accurately the boundaries of each source. With such information, it should then be possible to characterize the relative values of the efficiency parameter α for each source.

5.3. Variability of $\overline{\overline{AI}}$ Over Dust Sources

5.3.1. Daily Variation

[37] Figures 10 and 11 show the 1989 time series of TOMS AI and $\overline{\overline{AI}}$, and the corresponding local noon values of h_{PBL}, u_* and p_s over Afghanistan and the Bodele depression, respectively. The missing data are due to the low threshold of observed reflectivity (13%) and soil moisture (20%). The values of $\overline{\overline{AI}}$ reproduce most of the daily and seasonal variability. Similar comparisons exist for the other years and the other sources. These comparisons can also be seen as a validation of GEOS DAS surface meteorological fields over arid regions.

5.3.2. Seasonal Variation

[38] Table 2 gives, for 13 dust sources, the number of months when the observed reflectivity and soil moisture are lower than 20%, followed by the correlation coefficient R between the monthly mean TOMS AI and empirical $\overline{\overline{AI}}$, calculated with daily values from equation (13). There is a 99.999% probability of correlation for all sources. Figure 12 shows the comparison for Afghanistan and Bodele depression of the monthly TOMS AI and empirical $\overline{\overline{AI}}$ from 1981 to 1990, considering four cases: (1) $\overline{\overline{AI}} \sim 1.25 + 5\ (1 - \omega_{380})\ h_{PBL}$, (2) $\overline{\overline{AI}} \sim (u_*(1 - (\frac{u_t}{u_*})^2))^{\omega_{380}}$, (3) $\overline{\overline{AI}} \sim (1.25 + 5\ (1 - \omega_{380})h_{PBL}) \times (u_*(1 - (\frac{u_t}{u_*})^2))^{\omega_{380}}$, and (4) $\overline{\overline{AI}} \sim A(1 - 0.2 \log(p_s)) \times (1.25 + 5(1 - \omega_{380})h_{PBL}) \times (u_*(1 - (\frac{u_t}{u_*})^2))^{\omega_{380}}$, with ω_{380} = 0.75 and 0.85 for Afghanistan and Bodele depression, respectively. The four seasons have been separated using different symbols. The highest correlation is obtained with relation (13) depending on h_{PBL}, u_*, and p_s. The lowest correlation is with case 2 (dependency on u_*) which indicates the high sensitivity of TOMS AI to the altitude. The weakest dependency is on p_s which is mostly important for elevated sources (e.g., Taklamakan). In Afghanistan, the maximum values of $\overline{\overline{AI}}$ are in summer and correspond to the maximum of the elevation and surface wind speed. The slope of the regression line in the far right panel is close to 1 which means that the constant A = 1 in relation (13). The slope is around 0.3 for the Bodele depression but as discussed in section 4.3, the influence of active upstream sources bias the correlation. Such influence is apparent in the minimum value of TOMS AI which never get below 2. Then if $\overline{\overline{AI}}$ can reproduce correctly the seasonal variation it is because the emission of the upstream sources are in phase with our selected TOMS grid cell. This makes sense because the upstream sources are situated in the same depression and are subjected to similar meteorology. A question to ask is to what extent the improvement of correlation from case 1 to case 4 is related to the dust sources. In other words, is it possible to identify the dust sources by looking where are the highest increase of correlation.

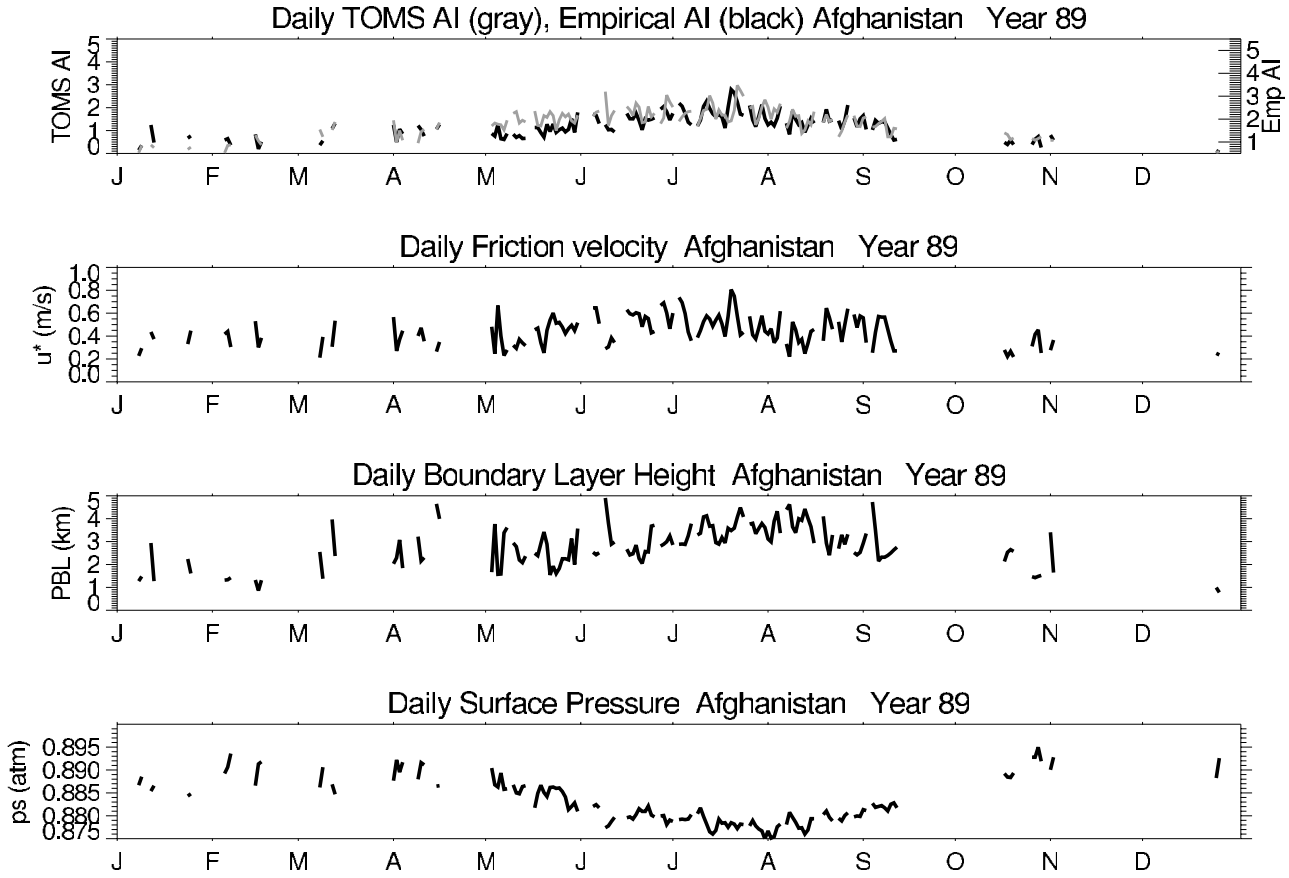

Figure 10. Daily variation of the TOMS AI and $\overline{\overline{AI}}$ (upper panel), the friction velocity (upper middle panel), the planetary boundary layer height (lower middle panel), and the surface pressure (lower panel) at local noon over Afghanistan in 1989.

Figure 13 shows the percentage of increase of correlation from case 1 to case 3 (no dependency on surface pressure) assuming $A = 1$, $u_t = 0$, and $\omega = 0.85$, everywhere. It is remarkable that most sources (including the 13 selected here) identified by *Prospero et al.* [2002] appear on this figure.

[39] Figure 14 (left panels) shows, for Afghanistan and the Bodele depression, the seasonal variation of the monthly TOMS AI (dashed line) and $\overline{\overline{AI}}$ (continuous line) and their standard deviation. As can be seen from the plots on Figure 14, the amplitude variation of the TOMS AI and its standard deviation are well reproduced with the empirical $\overline{\overline{AI}}$. Figure 14 (right panels) shows the seasonal variation of the terms depending on u_* and h_{PBL}. Over Afghanistan, it appears that most of the seasonal variation of the TOMS AI is due to variation in boundary layer height. The peak of TOMS AI in July corresponds to the peak of h_{PBL}, while the term in u_* has its maximum in May. Over the Bodele depression, the influence of h_{PBL} is less pronounced and u_* is producing most of TOMS AI variability.

5.3.3. Interannual Variation

[40] Figure 15 shows the interannual variation of the monthly values of TOMS AI and $\overline{\overline{AI}}$, and of the percentage variation of the monthly anomalies of u/ast and h_{PBL}. The interannual variation of TOMS AI is relatively well reproduced with $\overline{\overline{AI}}$ for both Afghanistan and the Bodele depression. The interannual variation is relatively weak and can be explained by the the percentage variation of u_* and h_{PBL} which are within 20%, except for a few cases. In August 1986, there is a maximum of u_* over Afghanistan which creates a maximum in $\overline{\overline{AI}}$ but is not observed by TOMS AI. Over the Bodele depression the maximum u_* is in April 1987 and corresponds to a maximum of both $\overline{\overline{AI}}$ and TOMS AI. For the other sources the anomalies are also within 20%, and the mean values for each source are given in Table 2. An exception is in Mauritania where the percentage variation of h_{PBL} is as high as 400% but these exceptional cases are in winter when h_{PBL} is too low to have an impact on $\overline{\overline{AI}}$. An interesting application of our method would be to relate the interannual variability of $\overline{\overline{AI}}$ and its terms with large scale oscillation, as it has been done for the TOMS AI and the North Atlantic Oscillation over the Atlantic by Chiapello and Moulin [2002].

5.4. Discussion

[41] It has been shown that $\overline{\overline{AI}}$ can reproduce most of the daily, seasonal and interannual variability of TOMS AI over major dust sources, and they are related to h_{PBL} and u_*. We have shown that in the case of the Bodele depression the upstream sources have a significant influence on the dust loading over the selected grid box. However, such influence modifies the absolute value of TOMS AI but not its variability. The reason is that the activity of these upstream

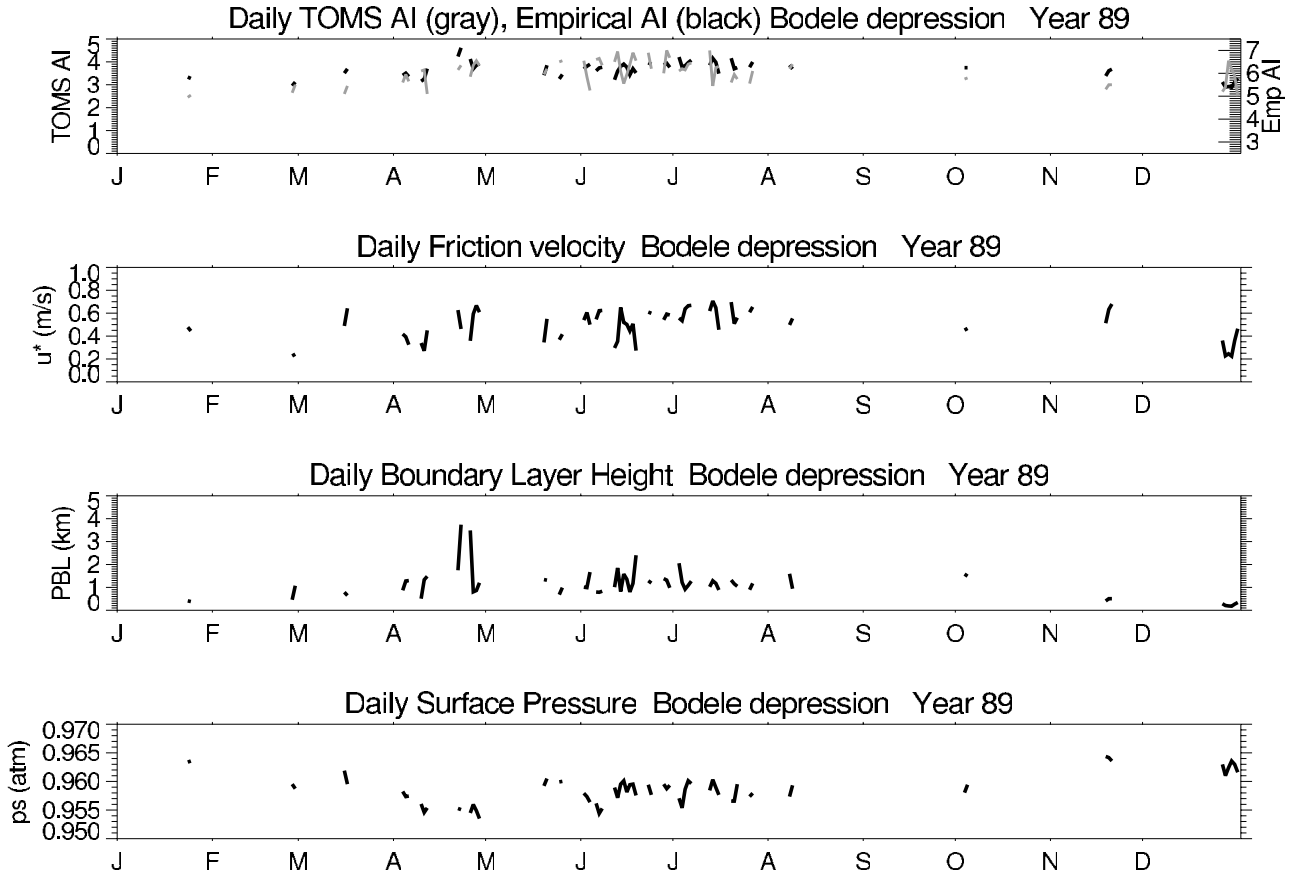

Figure 11. Daily variation of the TOMS AI and $\overline{\overline{AI}}$ (upper panel), the friction velocity (upper middle panel), the planetary boundary layer height (lower middle panel), and the surface pressure (lower panel) at local noon over the Bodele depression in 1989.

sources is in phase with the one in the selected grid box. A better way, to solve this would be to include a divergence term which takes into account the lateral fluxes. The relation $m = \frac{Q}{v_d}$ should be replaced by

$$\frac{\partial m}{\partial t} = Q - v_d m + \nabla(\bar{u}m) \tag{14}$$

The divergence term $\nabla(\bar{u}m)$ will be significant compared to the flux Q and deposition v_d if there is a strong gradient in the winds u or mass m. Generally, the sources are located in topographic depressions [cf. *Prospero et al.*, 2002], and it is possible that the gradients of both u and m are significant. If there is complete blocking in one side of the cell, the divergence will be proportional to u, or similarly u_*. We have seen that Q depends on u_*^3 and v_d on u_*^2. The sensitivity analysis in section 6.1 indicates that TOMS AI is linearly related to u_*. Therefore, the relation (13) is generally valid for all sources or the divergence term is dominant in equation 14. The only possibility to evaluate the relative weight of each term in equation 14 is to use a three-dimensional transport model. But the task will necessitate to define accurately the boundaries of each source and to take into account the effects of topography. The resolution of such model will be prohibitive and the dynamic poorly constrained by observations. An intermediate solution would be to consider plume models which are widely used to calculate pollutants dispersion. The advantage of such models is that it is possible to take into account transport with an analytical solution. It would then be possible to consider contamination between sources and to obtain more accurate results.

[42] Concerning the use of the empirical TOMS index to characterize the sources of other absorbing aerosols, a key aspect is the dependency of the imaginary part of the refractive index (absorption) with wavelength. A spectral dependency can compensate the reduced sensitivity with altitude of TOMS AI, as for the case of dust. For carbonaceous aerosols, the absorption is spectrally flat [*Dubovik et al.*, 2002] and the TOMS Index is reduced to near zero or negative values for near surface smoke plumes, as discussed by *Torres et al.* [1998].

6. Conclusions

[43] An empirical relation has been developed to express the TOMS Aerosol Index, for dust aerosol, as a function of four physical quantities: the single scattering albedo, optical thickness, altitude of the aerosol plume and surface pressure. This relation provides for the first time a quantitative relation between the TOMS AI and physical quantities which is applied (1) to validate simulated dust distribution, and (2) to characterize the dust sources. An example of application is shown for Saharan dust plume forming complex patterns over the North Atlantic in March 1988. The second application relates TOMS AI with the surface meteorological fields for the case of dust sources. It is assumed that dust concentration is at equilibrium between

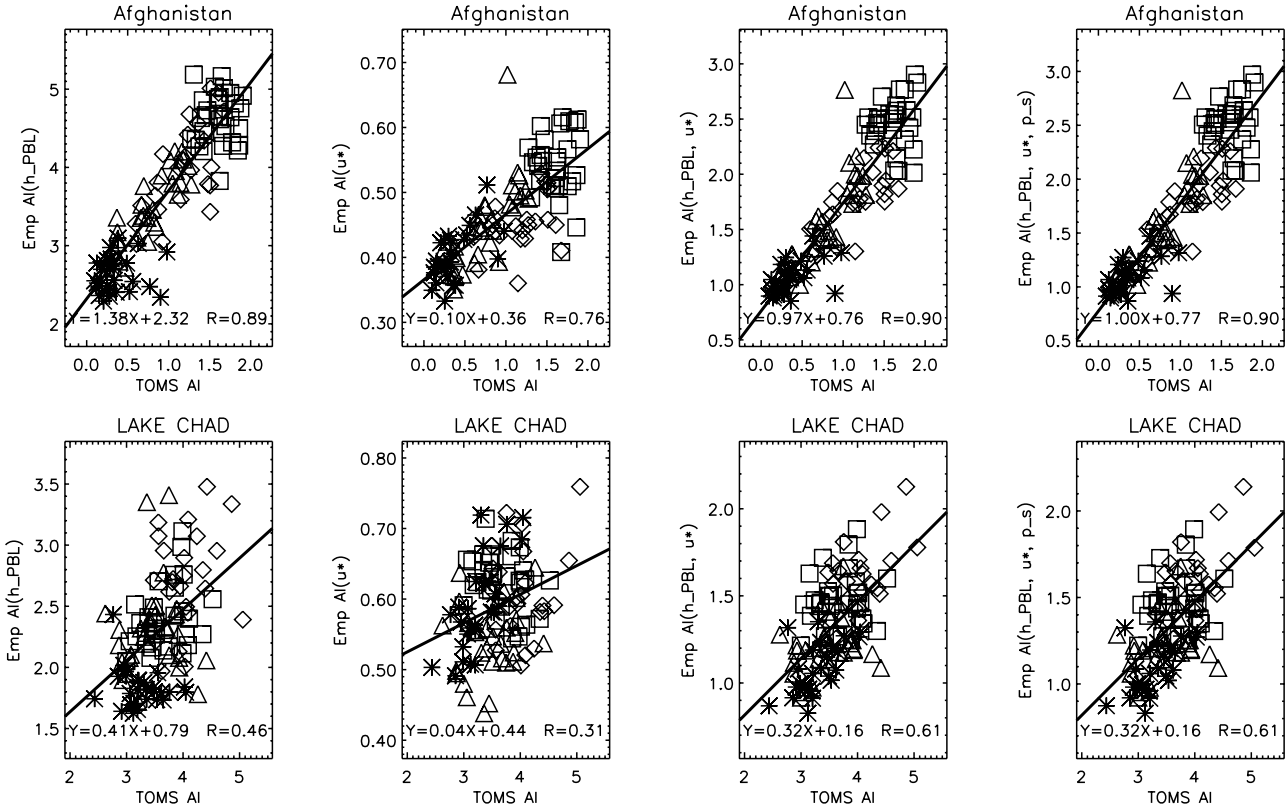

Figure 12. Comparison of the monthly TOMS AI and $\overline{\overline{AI}}$ considering four dependencies (see text) for Afghanistan (upper panels) and Bodele depression (lower panels), with the season indicated by different markers: Dec–Jan–Feb (stars), Mar–Apr–May (diamonds), Jun–Jul–Aug (squares), and Sep–Oct–Nov (triangles).

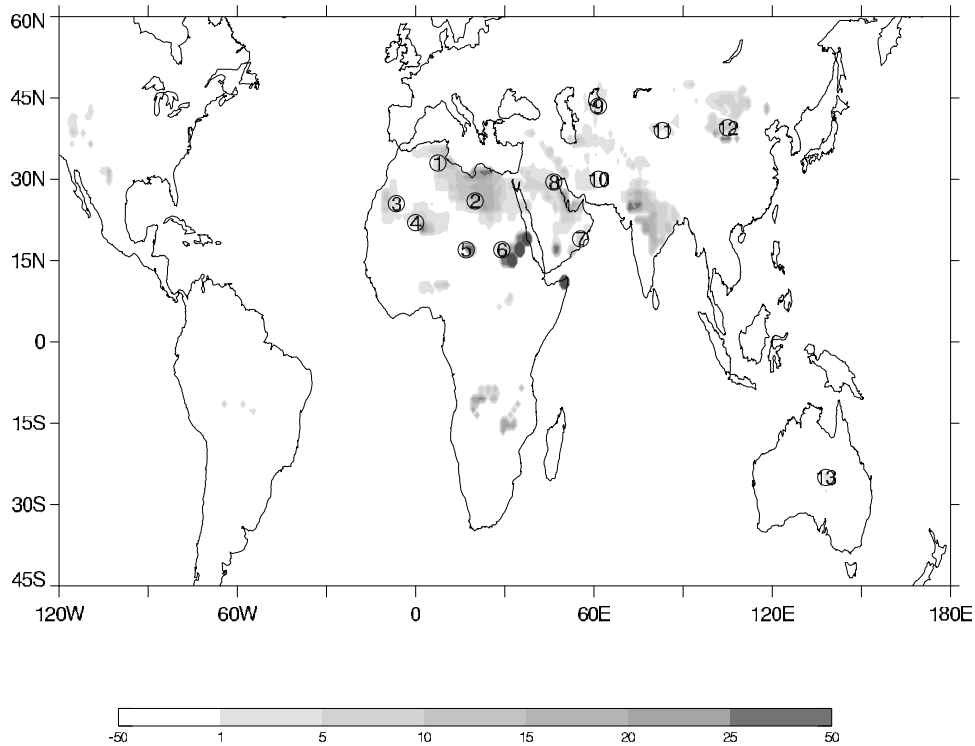

Figure 13. Global distribution of the relative difference of correlation between a unique dependency on h_{PBL} and on both h_{PBL} and u_* as in relation (13).

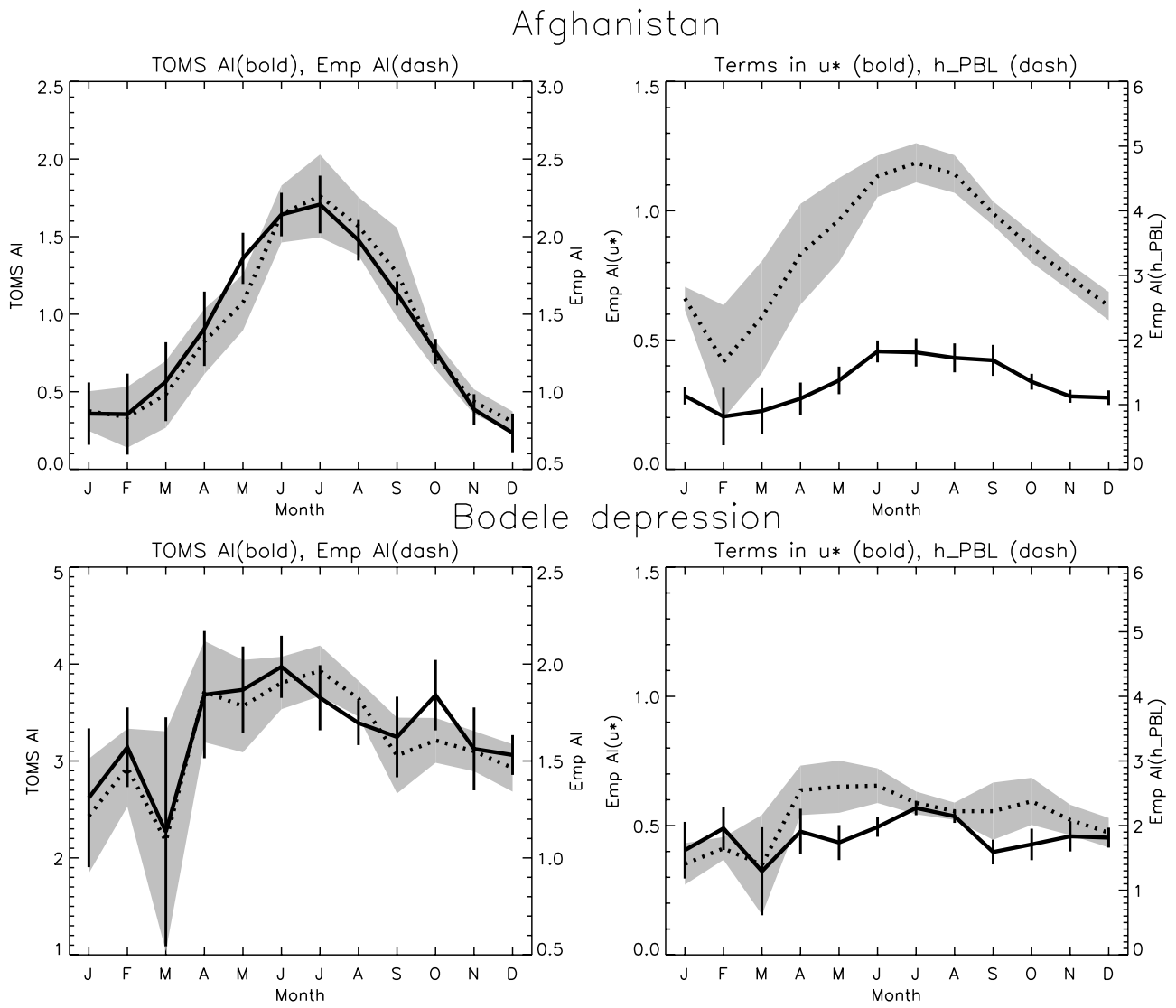

Figure 14. Comparison of the monthly TOMS AI (black line) and $\overline{\overline{AI}}$ (dash line), in the left panels, and the corresponding variation of the terms in u_* (black line) and in h_{PBL} (dash line), in the right panels, for Afghanistan (upper panels) and Bodele depression (lower panels).

the emission and deposition. With such assumption the dust concentration is proportional to the friction velocity. The altitude of the dust plume is assumed to correspond to the planetary boundary layer height. There are three degrees of freedom in the second relation: the single scattering albedo, the threshold velocity for wind erosion and the size distribution. Using daily local noon values over 10 years of the analyzed meteorological fields from GEOS DAS and the observed TOMS AI, the best estimated values of the three degrees of freedom are evaluated. However the errors inherent to our method does not allow to retrieve the threshold velocity. A different method is proposed for that purpose. The mean particle radius is estimated between 10 and 14 μm, which is in agreement with in situ data of falling particles during dust storms in Mali. The second relation is sensitive to the single scattering albedo and the estimated values are similar to published data, although our method is subject to large errors. These errors have been analyzed in details for two sources (Afghanistan and Bodele depression). They are associated with the weak sensitivity of the TOMS instrument to absorbing aerosols near the surface, the coarse resolution of the TOMS and meteorological fields, and the contamination from upstream sources. Despite these errors, the correlation between the daily, seasonal and interannual TOMS AI and $\overline{\overline{AI}}$ is surprisingly high. When considering separately the dependency on the plume altitude, the friction velocity, and the surface pressure, the highest correlation is obtained when they are all three combined. The spatial distribution of such correlation coefficient shows that its maxima are located where major dust sources have been identified by *Prospero et al.* [2002].

[44] Our methodology has the advantage to use a simple model but contains large errors. It is not obvious that more elaborate models could provide more accurate results mainly because of the poor characterization of the meteorological fields in arid or semi-arid regions. Also, to simulate accurately the generation and transport of dust plumes would necessitate a numerical resolution which would be prohibitive. The advances in satellite resolution could provide more robust parameterization once it would be possible to retrieve

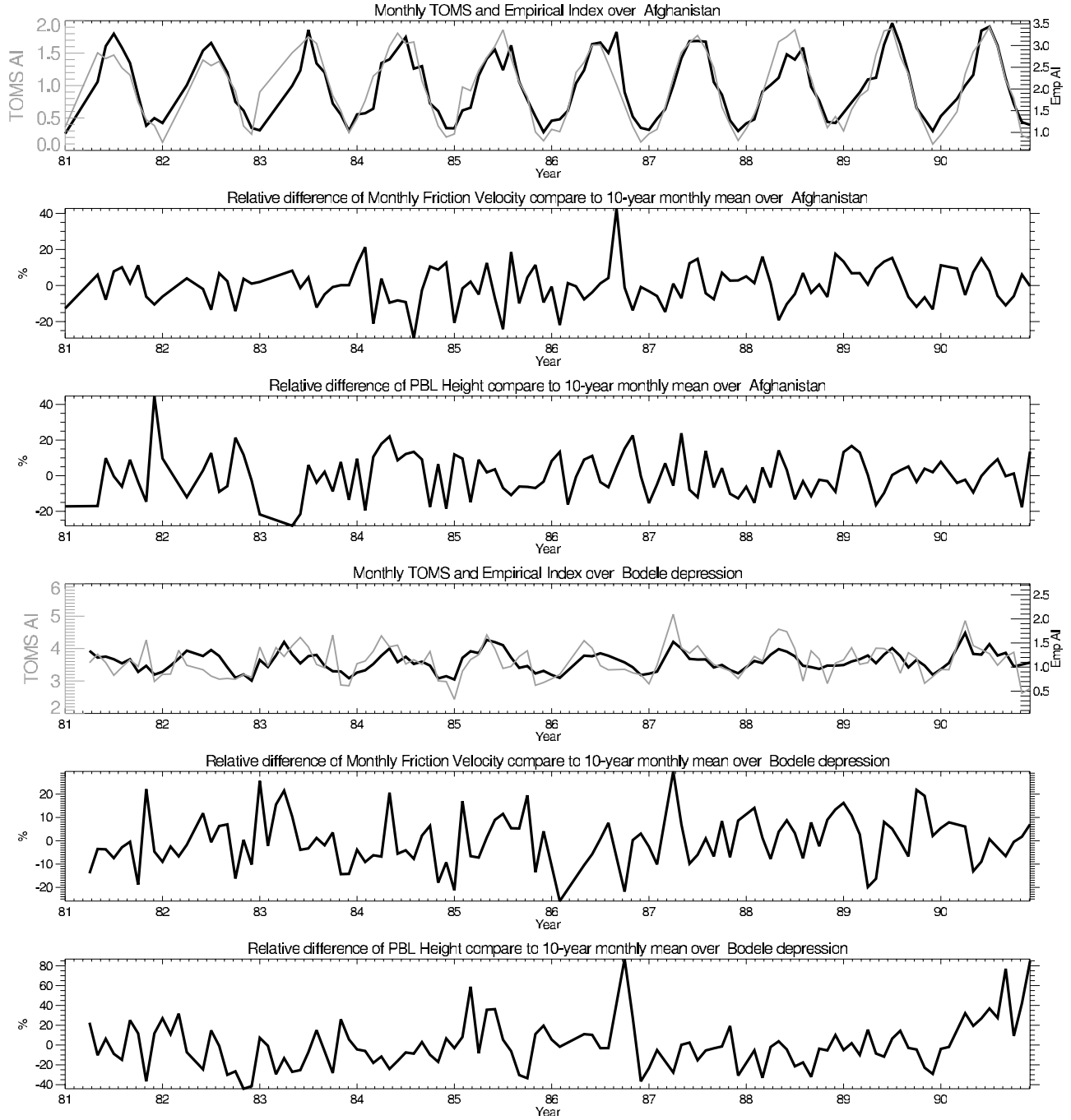

Figure 15. Comparison of the interannual variation of TOMS AI (gray line) and $\overline{\overline{AI}}$ (black line) for Afghanistan (upper panel) and Bodele depression (fourth panel), and the corresponding percentage difference of monthly friction velocity and 10-year monthly mean of u_* (second and fifth panels) and h_{PBL} (third and sixth panels).

aerosol properties over deserts from MODIS or SeaWiFS data.

Appendix A: Approximation of Dry Deposition

[45] Following *Slinn* [1982], the dry deposition velocity can be expressed as

$$v_d = v_g + \frac{1}{R_a + R_s}, \tag{A1}$$

where v_g is the gravitational settling velocity, R_a is the aerodynamic resistance and R_s is the quasi-laminar resistance.

[46] The gravitational settling is calculated as

$$v_g = \frac{1}{18}\frac{d_p^2 \rho_p g C_C}{\mu} \tag{A2}$$

where d_p is the particle diameter, ρ_p is the particle density, g is the acceleration of gravity, μ is the absolute viscosity of

the air (1.72 10^{-5} kg m^{-1} s^{-1}), and C_C is the Cunningham correction. For coarse particles $C_C = 1$ is a good approximation. Assuming a volume size distribution, typical for African desert, with a 17 μm mean diameter and a density $\rho_p = 2500$ kg m^{-3} then the gravitational settling speed $v_g \sim 2\ 10^{-2}$ m s^{-1}.

[47] The aerodynamic resistance, R_a, is a function of the atmospheric surface layer stability. Under neutral or unstable conditions, R_a is relatively low compare to R_s [*Seinfeld and Pandis*, 1998]. Over desert area around noon, the surface layer is strongly unstable, $R_a \sim 10^{-4}$ s m^{-1}, and R_a can be neglected.

[48] The quasi-laminar resistance for aerosols is given by

$$R_s = \frac{1}{\epsilon_0 u* (Sc^{-\gamma} + 10^{-3/St})}, \tag{A3}$$

where $\epsilon_0 = 3$ is an empirical constant, *Sc* is the Schmidt number, $\gamma = 0.5$ for deserts [*Slinn and Slinn*, 1980], and *St* is the Stanton number. The Schmidt number is given by the ratio of the kinematics viscosity, ν, and the Brownian diffusivity, *D*. The kinematic viscosity ν is related to the dynamic viscosity by the relation $\nu = \mu/\rho_a$ with $\rho_a = 1.225$ kg m^{-3} the air density. The diffusivity *D* is given by

$$D = \frac{kT}{3\pi\mu d_p} \tag{A4}$$

where $k = 1.38\ 10^{-23}$ J K^{-1} is the Boltzmann constant and *T* is the temperature. At ambient temperature, 300 K, the diffusivity $D \sim 5\ 10^{-12}$ m^2 s^{-1} and the Schmidt number $Sc \sim 8.5\ 10^7$.

[49] The Stanton number St for a smooth surface is given by [*Giorgi*, 1986],

$$St = \frac{v_g u_*^2}{\nu g} \tag{A5}$$

Using $v_g = 2\ 10^{-2}$ m s^{-1}, $\nu = 1.4\ 10^{-5}$ m^2 s^{-1}, and $g = 9.81$ m s^{-2}, then $St \sim 150\ u_*^2$. After substituting the value of the different parameters in equation (A3), the quasi laminar resistance R_s is approximated by

$$R_s \sim \frac{1}{3u* \left(3.410^{-4} + 10^{-\frac{0.02}{u_*^2}} \right)} \tag{A6}$$

The second term of the denominator varies almost linearly with $u*$ for $u* > 0.1$ m s^{-1}, and the first term is negligible. Finally, the deposition velocity for a 17 μm effective diameter, v_{d17} is approximated by $v_{d17} \sim 210^{-2} + 3\ u_*^2$ which is further simplified into

$$v_{d17} \sim 3u_*^2. \tag{A7}$$

[50] **Acknowledgments.** The authors thank the TOMS OPT team for producing the TOMS aerosol data set, Andrea Molod for her help in using DAO data and Richard Rood to give us access to these data. We are grateful to Peter Colarco for his comments on the manuscript. This work is partially supported by NASA grant NAG-35-694.

References

Alpert, P., S. O. Krichak, M. Tsidulko, H. Shafir, and J. H. Joseph, A dust prediction system with TOMS initialization, *Mon. Weather Rev.*, *130*, 2335–2345, 2002.

Bounoua, L., and T. N. Krishnamurti, Thermodynamic budget of the five day wave over the Saharan desert during summer, *Meteorol. Atmos. Phys.*, *47*, 1–25, 1991.

Chiapello, I., and C. Moulin, TOMS and METEOSAT satellite records of the variability of Saharan dust transport over the Atlantic during the last two decades (1979–1997), *Geophys. Res. Lett.*, *29*(8), doi:10.1029/2001GL013767, 2002.

Chin, M., R. B. Rood, S.-J. Lin, J.-F. Müller, and A. Thompson, Atmospheric sulfur cycle simulated in the global model GOCART: Model description and global properties, *J. Geophys. Res.*, *105*, 24,671–24,687, 2000.

Colarco, P. R., O. B. Toon, O. Torres, and P. J. Rasch, Determining the UV imaginary index of refraction of Saharan dust particles from TOMS data using a three-dimensional model of dust transport, *J. Geophys. Res.*, *107*(D16), doi:10.1029/2001JD000903, 2002.

Dentener, F. J., G. R. Carmichael, Y. Zhang, J. Lelieveld, and P. J. Crutzen, Role of mineral aerosol as a reactive surface in the global troposphere, *J. Geophys. Res.*, *101*, 22,869–22,889, 1996.

Dickerson, R. R., S. Kondragunat, G. Stenchikov, K. L. Civerolo, B. G. Doddridge, and B. N. Holben, The impact of aerosols on solar ultraviolet radiation and photochemical smog, *Science*, *278*, 827–830, 1997.

Dubovik, O., B. Holben, T. F. Eck, A. Smirnov, Y. J. Kaufman, M. D. King, D. Tanré, and I. Slutsker, Variability of absorption and optical properties of key aerosol types observed in worldwide locations, *J. Atmos. Sci.*, *59*, 590–608, 2002.

Fécan, F., B. Marticorena, and G. Bergametti, Parameterization of the increase of the aeolian erosion threshold wind friction velocity due to soil moisture for arid and semi-arid areas, *Ann. Geophys.*, *17*, 149–157, 1999.

Gillette, D. A., J. Adams, A. Endo, D. Smith, and R. Kihl, Threshold velocities for input of soil particles into the air by desert soils, *J. Geophys. Res.*, *85*, 5621–5630, 1980.

Gillies, J. A., W. G. Nickling, and G. H. McTainsh, Dust concentrations and particle-size characteristics of an intense dust haze event: Inland delta region, Mali, West Africa, *Atmos. Environ.*, *30*, 1081–1090, 1996.

Ginoux, P., M. Chin, I. Tegen, J. M. Prospero, B. Holben, O. Dubovik, and S. J. Lin, Sources and distributions of dust aerosols simulated with the GOCART model, *J. Geophys. Res.*, *106*, 20,255–20,274, 2001.

Ginoux, P., J. M. Prospero, O. Torres, and M. Chin, Long-term simulation of dust distribution with the GOCART model: Correlation with the North Atlantic Oscillation, *Environ. Model. Software*, doi:10.1016/S1364-8152(03)00114-2, in press, 2003.

Giorgi, F., A particle dry-deposition parameterization scheme for use in tracer transport model, *J. Geophys. Res.*, *91*, 9794–9806, 1986.

Herman, J. R., and E. Celarier, Earth surface reflectivity climatology at 340 and 380 nm from TOMS data, *J. Geophys. Res.*, *102*, 12,059–12,076, 1997.

Herman, J. R., P. K. Bhartia, O. Torres, C. Hsu, C. Seftor, and E. Celarier, Global distribution of UV-absorbing aerosols from Nimbus 7/TOMS data, *J. Geophys. Res.*, *102*, 16,911–16,922, 1997.

Hsu, N. C., J. R. Herman, O. Torres, B. N. Holben, D. Tanré, T. F. Eck, A. Smirnov, B. Chatenet, and F. Lavenu, Comparisons of the TOMS aerosol index with Sun photometer aerosol optical thickness: Results and applications, *J. Geophys. Res.*, *104*, 6269–6279, 1999.

Hsu, N. C., J. R. Herman, and C. Weaver, Determination of radiative forcing of Saharan dust using combined TOMS and ERBE data, *J. Geophys. Res.*, *105*, 20,649–20,661, 2000.

Karyampudi, V. M., and T. N. Carlson, Analysis and numerical simulations of the Saharan air layer and its effect on easterly wave disturbances, *J. Atmos. Sci.*, *45*, 3102–3136, 1988.

Karyampudi, V. M., et al., Validation of the Saharan dust plume conceptual model using lidar, Meteosat, and ECMWF data, *Bull. Am. Meteorol. Soc.*, *80*, 1045–1076, 1999.

Kinne, S., et al., Monthly averages of aerosol properties: A global comparison among models, satellite data, and AERONET ground data, *J. Geophys. Res.*, *108*, doi:10.1029/2001JD001253, in press, 2003.

Liao, H., Y. L. Yung, and J. H. Seinfeld, Effects of aerosols on tropospheric photolysis rates in clear and cloudy atmospheres, *J. Geophys. Res.*, *104*, 23,697–23,707, 1999.

Marticorena, B., and G. Bergametti, Modeling the atmospheric dust cycle: 1. Design of a soil-derived dust emission scheme, *J. Geophys. Res.*, *100*, 16,415–16,430, 1995.

Martin, J. H., and R. M. Gordon, Northeast Pacific iron distributions in relation to phytoplankton productivity, *Deep Sea Res.*, *35*, 177–196, 1988.

Martin, R. V., et al., Interpretation of TOMS observations of tropical tropospheric ozone with a global model and in situ observations, *J. Geophys. Res.*, *107*(D18), 4351, doi:10.1029/2001JD001480, 2002.

Patterson, E. M., D. A. Gillette, and B. H. Stockton, Complex index of refraction between 300 and 700 nm for Saharan aerosols, *J. Geophys. Res.*, *82*, 3153–3160, 1977.

Prospero, J. M., Long-term measurements of the transport of African mineral dust to the southeastern United States: Implications for regional air quality, *J. Geophys. Res.*, *104*, 15,917–15,927, 1999.

Prospero, J. M., R. Schmitt, E. Cuevas, D. L. Savoie, W. C. Graustein, K. K. Turekian, A. Volz-Thomas, A. Diaz, S. J. Oltmans, and H. Levy II, Temporal variability of summertime ozone and aerosols in the free troposphere over the eastern North Atlantic, *Geophys. Res. Lett.*, *22*, 2925–2928, 1995.

Prospero, J. M., P. Ginoux, O. Torres, S. Nicholson, and T. Gill, Environmental characterization of global sources of atmospheric soil dust derived from the Nimbus 7 Total Ozone Mapping Spectrometer (TOMS) absorbing aerosol product, *Rev. Geophys.*, *40*(1), 1002, doi:10.1029/2000RG000095, 2002.

Prospero, J. M., E. Blades, G. Mathison, and R. Naidu, Interhemispheric transport of viable fungi and bacteria from Africa to the Caribbean with soil dust, *Global Biogeochem. Cycles*, *17*, in press, 2003.

Schubert, S. D., R. B. Rood, and J. Pfaendtner, An assimilated data set for Earth science applications, *Bull. Am. Meteorol. Soc.*, *74*, 2331–2342, 1993.

Seinfeld, J. H., and S. N. Pandis, *Atmospheric Chemistry and Physics*, John Wiley, Hoboken, N. J., 1998.

Shao, Y., and L. M. Leslie, Wind erosion prediction over the Australian continent, *J. Geophys. Res.*, *102*, 30,091–30,105, 1997.

Shay-El, Y., P. Alpert, and A. da Silva, Reassessment of the moisture source over the Sahara Desert based on NASA reanalysis, *J. Geophys. Res.*, *104*, 2015–2030, 1999.

Sinyuk, A., O. Torres, and O. Dubovik, Combined use of satellite and surface observations to infer the imaginary part of refractive index of Saharan dust, *Geophys. Res. Lett.*, *30*(2), 1081, doi:10.1029/2002GL016189, 2003.

Slinn, W. G. N., Prediction for particle deposition to vegetative canopies, *Atmos. Environ.*, *16*, 1785–1794, 1982.

Slinn, W. G. N., and W. G. N. Slinn, Prediction for particle deposition on natural waters, *Atmos. Environ.*, *14*, 1013–1016, 1980.

Sokolik, I. N., and G. Golitsyn, Investigation of optical and radiative properties of atmospheric dust aerosols, *Atmos. Environ., Part A*, *27*, 2509–2517, 1993.

Sokolik, I. N., and O. B. Toon, Direct radiative forcing by anthropogenic airborne mineral aerosol, *Nature*, *381*, 681–683, 1996.

Sokolik, I. N., and O. B. Toon, Incorporation of mineralogical composition into models of the radiative properties of mineral aerosol from UV to IR wavelengths, *J. Geophys. Res.*, *104*, 9423–9444, 1999.

Tegen, I., and A. A. Lacis, Modeling of particle size distribution and its influence on the radiative properties of mineral dust aerosol, *J. Geophys. Res.*, *101*, 19,327–19,344, 1996.

Torres, O., P. K. Bhartia, J. R. Herman, Z. Ahmad, and J. Gleason, Derivation of aerosol properties from satellite measurements of backscattered ultraviolet radiation: Theoretical basis, *J. Geophys. Res.*, *103*, 17,099–17,110, 1998.

Torres, O., P. K. Bhartia, J. R. Herman, A. Sinyuk, P. Ginoux, and B. Holben, A long-term record of aerosol optical depth from TOMS observations and comparison to AERONET measurements, *J. Atmos. Sci.*, *59*, 398–413, 2002.

P. Ginoux, Geophysical Fluid Dynamics Laboratory, NOAA, Forrestal Campus, P.O. Box 308, Princeton, NJ 08542, USA. (paul.ginoux@noaa.gov)

O. Torres, NASA Goddard Space Flight Center, Code 916, Greenbelt, MD 20771, USA. (torres@tparty.gsfc.nasa.gov)